

Experimental investigation of the effects of floating wind turbine motion on a downstream turbine performance and loads

Alessandro Fontanella¹, Stefano Cioni², Francesco Papi², Sara Muggiasca¹, Alessandro Bianchini², and Marco Belloli¹

¹Department of Mechanical Engineering, Politecnico di Milano, via La Masa 1, 20156 Milano, Italy.

²Department of Industrial Engineering, Università degli Studi di Firenze, Via di Santa Marta 3, 50139 Firenze, Italy.

Correspondence: Alessandro Fontanella (alessandro.fontanella@polimi.it)

Abstract. This study investigates how the motion of a floating wind turbine affects the aerodynamic performance and dynamic loading of a downstream turbine operating in its wake. Wind tunnel experiments were conducted using a two-turbine setup, where the upstream turbine was subjected to controlled platform motions (both sinusoidal and wave driven) while the downstream turbine remained fixed and was tested in multiple relative positions. Results show that large-amplitude, low-frequency, sinusoidal motions of the upstream turbine, especially in crosswind and yaw directions, can increase the power output of the downstream turbine under low-turbulence conditions and at short turbine spacing (3-5 rotor diameters). The largest relative ~~power~~ gain reached 26% over the fixed case, although ~~absolute gains remained moderate~~ the absolute increase remained moderate because the highly persistent wake, driven by low turbulence and strong thrust of the upstream turbine, resulted in very low baseline power of the downstream turbine. The gains obtained under idealized sinusoidal motions were replicated in cases with realistic-wave-driven motions when wind and waves were aligned, but not when wind-wave misalignment introduced crosswind movements of the upstream wind turbine. In parallel, motion of the upstream turbine increased the dynamic loading on the waked turbine. Load increments varied with turbine spacing and alignment and were more pronounced in sinusoidal motion cases than with wave-induced motions, which also produced increased dynamic loading but with smaller amplitudes. The loads resulting from wave-induced motions exhibited a broad spectral distribution, consistent with the wide frequency content of the wave excitation. Overall, these findings underscore that platform-induced wake dynamics are not a secondary effect, but a key driver of wake recovery, downstream turbine performance, and dynamic loading, and must be considered in the design and operation of floating wind farms.

1 Introduction

The deployment of floating offshore wind farms is a key strategy to harness wind energy in deep-water regions where fixed-bottom turbines are not feasible. While the floating wind technology enables access to abundant yet untapped wind resources, it also introduces additional complexities, especially regarding system dynamics due to the large motions of platforms and their influence on the wind turbine aerodynamic response. In particular, the aerodynamic interactions between wind turbines through wakes, which is already a critical factor in bottom-fixed wind farms, become even more complex in floating wind

farms, as the aforementioned large platform motions may lead to more unsteady and irregular wake flows. These wake effects
25 alter power generation, fatigue loading, and control requirements at the turbine and plant levels. Despite their importance, they
remain poorly understood (Meyers et al., 2022) and one reason for the limited understanding of aerodynamic interactions in
floating wind farms is the lack of wake and performance data from operational plants. In fact, to date, only a few floating wind
farms have been constructed, each comprising a small number of turbines (Chitteth Ramachandran et al., 2022).

The motion of a floating wind turbine under environmental forcing is characterized by two distinct frequency ranges. Motions
30 at different frequencies are known to produce different aerodynamic responses (Schulz et al., 2024, 2025), thus the frequency
content of the motion is an important factor to consider as it can significantly influence wake development. Ocean waves
typically excite the platform at frequencies between 0.05 and 0.2 Hz; the tower-top motion amplitude resulting from this
forcing depends on both platform characteristics and sea state. At lower frequencies, the platform eigenmodes are excited by
wind turbulence and wave forcing which may induce a response through nonlinear effects. These lower-frequency motions
35 can lead to response amplitudes substantially larger than those in the wave-frequency range; the amplitude of this response
is again influenced by platform characteristics, wind, and sea state. Considering both frequency ranges, the realistic range for
rotor reduced frequencies (the ratio of the product of frequency and rotor diameter to wind speed) spans from slightly less than
1 to 10 (Schulz et al., 2025).

Most available studies focus on the wake behavior of individual floating turbines and do not address how turbines interact
40 through wakes within a full wind farm. A recent study by Angelou et al. (2023) examined the far wake of a 6 MW floating
wind turbine in the Hywind Scotland offshore wind farm, the world's first floating wind farm, using LiDAR measurements.
Its findings indicate that, under mild wave excitation causing small-amplitude platform motions, the wakes of floating turbines
have time-averaged characteristics similar to those of fixed-bottom turbines. Under these conditions, atmospheric turbulence
was identified as the dominant mechanism for wake recovery, with platform motion having a negligible effect. However, the
45 investigation focused on conditions in which the turbine operated outside the wake of upstream units, and therefore did not
address the impact of upstream wakes on turbine performance within the array.

The impact of platform motions on the wake behavior of floating wind turbines has been extensively investigated through
wind tunnel experiments, which offer controlled and repeatable conditions ideal for isolating aerodynamic phenomena. Most
of these studies have used model-scale wind turbines in a low-turbulence inflow, subjecting them to ~~unidirectional sinusoidal~~
50 ~~motions~~sinusoidal motions, typically prescribed in one degree of freedom at a time. The investigated motions ~~typically~~generally
had relatively large amplitudes and low frequencies, with reduced frequencies up to 1.5. This range is representative of both
the eigenmode responses of floating wind turbines and the lower end of the wave-frequency spectrum. The amplitudes were
selected to create tower-top motions ranging from 2% to 10% of the rotor diameter.

The experiment of Bayati et al. (2017a) analyzed the effect of surge motion on the near wake of a 1:75 scale model of the
55 DTU 10 MW wind turbine (Bak et al., 2013), demonstrating that platform motion introduces wind speed fluctuations in the
wake. Building on this, Fontanella et al. (2022b) explored additional surge motion conditions and showed how motion affects
the formation and evolution of tip vortices near the rotor. In a later study, Fontanella et al. (2022a) investigated the wake of a
1:100 scale model of the IEA 15 MW reference turbine (Gaertner et al., 2020) under platform motions in along-wind and cross-

wind directions; the results indicated that all motion types induced velocity fluctuations in the wake, although mean velocity
60 in the near wake was slightly reduced compared to the fixed-turbine case. Messmer et al. (2024a) further examined wake
behavior under harmonic surge and sway motions in laminar inflow conditions. The study found that sway motion enhances
lateral meandering, while surge motion induces wake pulsation; both contribute to improved mixing and recovery of the far
wake. In a follow-up study, Messmer et al. (2024b) assessed the effect of surge motion under inflow turbulence intensities up
to 3%, showing that increased turbulence significantly diminishes the influence of platform motion on the far wake recovery.

65 A notable exception to the wind tunnel studies that focused on individual turbines is presented in the work of Bossuyt
et al. (2023), which investigated a 1:400-scale floating wind farm with twelve turbines in a wind–water tunnel under a sheared
inflow with 10% turbulence intensity and wave excitation. Despite the challenges of simultaneously scaling aerodynamics and
hydrodynamics, the study revealed clear differences in wake recovery linked to periodic rotor motions: wave-induced yaw and
pitch led to synchronized vertical wake oscillations that enhanced recovery but also increased turbulence levels, potentially
70 affecting the unsteady loading on downstream turbines.

Taken together, these experiments consistently demonstrate that large rotor motions influence wake development, generating
flow structures with the same periodicity as the platform motion. These dynamic features, primarily seen as pulsations in
velocity and increased lateral meandering, are absent in wakes of bottom-fixed turbines. Under nearly laminar conditions,
such wake dynamics can enhance recovery, but their effect becomes negligible as inflow turbulence increases. At low but
75 realistic turbulence intensities, platform motions still generate coherent periodic structures, but they do not lead to substantial
improvements in wake recovery.

The limited availability of experimental data has led to diverse modeling approaches for floating wind farms, often yielding
scattered results. Carmo et al. (2024) used FAST.Farm, which neglects dynamic wake effects due to platform motion, modeling
only the wake vertical deflection due to average rotor inclination. This simplification was deemed acceptable under typical
80 turbulence conditions, where wake pulsing effects are expected to be minimal. In contrast, Ramos-García et al. (2022) used a
vortex-multibody solver to show that platform motions in an upstream turbine enhance wake breakdown, increasing power and
thrust in downstream turbines and that this effect diminishes with higher inflow turbulence. Simulations with prescribed surge
and pitch motions confirmed that platform dynamics significantly affect wake behavior and loading of downstream turbines,
especially deeper in the array where resonant interactions may occur.

85 A number of numerical studies using computational fluid dynamics (CFD) have investigated wake behavior in floating
wind turbines, often focusing on isolated machines (Micallef and Rezaeiha, 2021). Moving toward farm-scale interactions,
Arabgolarcheh et al. (2023) used unsteady Reynolds-averaged Navier–Stokes (URANS) simulations to examine the effect of
prescribed surge motion on two aligned floating wind turbines. Although the mean thrust and power output of the upstream
rotor were nearly unchanged between the fixed and surging scenarios, the motion generated periodic wake structures that
90 increased the dynamic loading on the downstream turbine. Li et al. (2025) used large-eddy simulations (LES) to investigate
wake interactions between two surging NREL 5 MW wind turbines (Jonkman et al., 2009), considering a motion amplitude
of 3% of the rotor diameter and a frequency of 0.1 Hz (reduced frequency 1.1), representative of typical wave conditions.
They found that, under laminar inflow, the power of the downstream turbine increased significantly. However, under inflow

with a turbulence intensity of 5.3%, this gain became negligible. Additional insight into the physical mechanisms governing this behavior has recently been provided by Pagamonci et al. (2025), who conducted LES-based CFD simulations on the same wind tunnel-scale turbine used in the present study. Their results show that, under turbulent inflow, the coherent flow structures induced by platform motion dissipate more rapidly than in laminar conditions, thereby reducing the associated gains in wake recovery.

Although CFD studies provide valuable insights into wake dynamics and turbine interactions, their results often vary due to differences in turbulence modeling, inflow conditions, and domain size. This variability limits their reliability in predicting wake effects in realistic floating farm configurations. This motivates the need for controlled experimental data, which can serve both to understand key physical mechanisms and to validate or calibrate numerical tools.

This study investigates, through wind tunnel experiments, how wakes generated by floating wind turbines affect the dynamic loading and power output of a downstream turbine operating in their wake. Building on previous numerical and experimental studies that suggested such effects are possible, the present work aims to quantify and characterize them under controlled experimental conditions. Specifically, it seeks to address the following questions:

1. To what extent, and under which conditions, do the unsteady flow disturbances induced by platform motion propagate downstream and influence the load response of a waked turbine?
2. How much, and under which conditions, can a turbine operating in the wake of a moving upstream rotor extract more power than one operating behind a bottom-fixed turbine?

The experiment and its results are presented in the following sections. Section 2 describes the methodology of the study, including the experimental setup, the operating conditions of the wind turbines, and the platform motions. Section 3 presents and analyzes experimental results. In Section 4, these results are discussed with the aim of evaluating their relevance and applicability to the design and operation of floating wind farms. This discussion also considers the limitations and simplifications inherent to the experimental setup. Finally, Section 5 summarizes the main findings of the study and outlines the conclusions.

2 Methodology

The experimental campaign was conducted in the atmospheric-boundary layer test section of Politecnico di Milano wind tunnel, which is 13.84 m wide by 3.84 m high by 35 m long and used two wind turbines (WT) that are 1:75 scale models of the DTU 10 MW reference wind turbine (Bak et al., 2013). In the experiment, the flow speed was scaled by a factor 1:3 compared to a full-scale environment. The time scaling in the experiment was determined by the geometric and velocity scales, resulting in a time scale ratio of 1:25. Consequently, the wind farm response in the experiment occurred 25 times faster than at full scale.

In the experiment, only the upstream turbine (WT1) was subjected to platform motions representative of a floating wind turbine, while the downstream turbine (WT2) was fixed at the tower base. This approach avoids introducing additional variables that could make it more difficult to identify the specific influence of the upstream turbine dynamics on the downstream turbine response. Similar methodologies have been employed in previous wind tunnel studies on wake interactions, particularly in

active wake control research, where only the most upstream turbine is dynamically actuated, and downstream turbines are operated with fixed settings (Van Der Hoek et al., 2024; Van Der Hoek et al., 2024). Once the effects of upstream rotor motion are well understood, the analysis can be extended to more realistic scenarios that also include the motion of the downstream turbine.

130 The experiment with two turbines followed the one of Fontanella et al. (2025b), that was performed in the same wind tunnel using the same wind turbine and robotic platform and measured the wake of the upstream wind turbine at the locations where WT2 was placed in the current experiment. Hence, the inflow caused by the wake of WT1 on the WT2 is precisely known because it has been already characterized.

2.1 Experimental setup

135 The experimental setup is shown in Fig. 1. The upstream wind turbine was mounted on a six-degrees-of-freedom robotic platform that mimics the rigid-body motions of floating foundations. The downstream wind turbine was mounted on a rigid support structure connecting the tower base to the wind tunnel floor.

The two wind turbines are identical, and their main geometric parameters are listed in Table 1. Each rotor has a diameter (D) of 2.38 m and was designed at a 1:75 scale with the primary objective of replicating the blade normal load distribution of
140 the DTU 10 MW reference turbine. Matching this distribution ensures that the model reproduces the thrust characteristics of the reference turbine with high accuracy and also leads to a reasonable match in power performance. Due to the reduced wind speed in the wind tunnel, the model operates at chord-based Reynolds numbers between 5×10^4 and 1.5×10^5 , well below the 10^6 – 10^7 range of the full-scale turbine. To achieve the target loads under these conditions, the rotor blades were specifically
145 designed for low-Reynolds-number operation. The SD7032 airfoil was selected for its favorable aerodynamic characteristics at such conditions: minimal lift sensitivity to Reynolds number for angles of attack below 10° , a linear lift curve, and no nonlinearities in drag (Fontanella et al., 2021). Based on this airfoil choice, the chord and twist distributions were adapted from those of the DTU 10 MW reference turbine (Bayati et al., 2017b). The aerodynamic performance of the resulting rotor is compared with that of the reference turbine in Appendix A.

~~The shaft of the wind turbines had a tilt of 5° , matching the full-scale version of the DTU 10 MW. During wind tunnel tests, the towers of the two wind turbines were tilted at a negative angle of 5° to ensure the rotors were vertical to the wind tunnel floor. This simplification was intended to limit the analysis to axial thrust and torque in scenarios without prescribed platform motion and with the turbine operating in undisturbed flow.~~

~~During the~~ The rotor tip was located approximately 0.5 m ($0.2D$) below the wind-tunnel ceiling. Previous studies on the same facility and turbine geometry have shown that this limited clearance can slightly constrain the vertical wake expansion, while leaving the qualitative wake behavior essentially unchanged (Bergua et al., 2023). Because the ceiling clearance is the same for all tested configurations, its influence is consistent across the campaign and does not hinder the comparison between fixed and moving-platform cases.

~~The shaft of the wind turbines had a tilt of 5° , matching the full-scale version of the DTU 10 MW. During wind tunnel tests, the towers of the two wind turbines were tilted at a negative angle of 5° to ensure the rotors were orthogonal to the wind tunnel~~

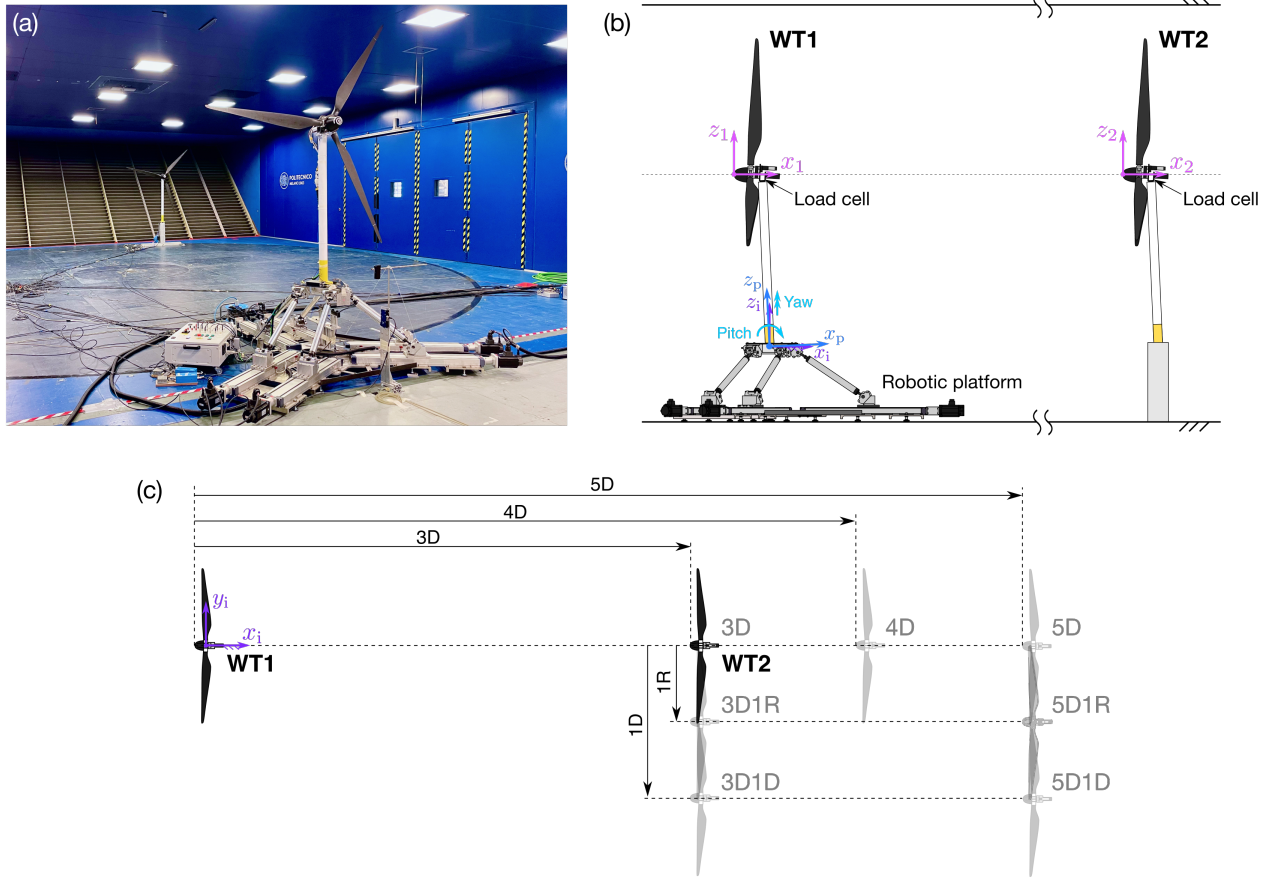


Figure 1. Experimental setup. (a): the two wind turbines in the wind tunnel, positioned at a distance of five rotor diameters (D), with a lateral offset of one radius (R). (b): schematic representation of the experimental setup with the coordinate systems. (c): wind farm configurations that were tested.

160 floor and to the incoming flow. This simplification was intended to limit the analysis to axial thrust and torque in scenarios without prescribed platform motion and with the turbine operating in undisturbed flow.

During the experiment, the position of WT2 relative to WT1 was varied to investigate how downstream distance and cross-wind offset influence the response of the downstream turbine, as illustrated in Fig. 1. WT2 was placed at downstream distances of $3D$, $4D$, and $5D$ along the same line as WT1. The maximum spacing was limited by the dimensions of the wind tunnel test section, which did not permit to place the downstream turbine beyond $5D$. While these spacings are shorter than those typically used in commercial wind farms, generally ranging from 6 to 10 rotor diameters (Stevens et al., 2017), they are particularly relevant for experimental investigation, as the dynamic wake behaviors induced by platform motion remain well-defined at these distances (Fontanella et al., 2025b; Firpo et al., 2024) and can significantly affect the performance and loading of downstream turbines. Studying these effects at short spacing helps isolate the impact of wake–motion interactions, providing insight into

Table 1. Geometry of the wind turbines used in the experiment.

Parameter	Unit	Value
Rotor diameter (D)	m	2.381
Blade length	m	1.102
Hub diameter	m	0.178
Hub height	m	2.190
Rotor overhang	m	0.139
Shaft tilt angle	°	5
Tower-to-shaft distance	m	0.064
Tower length	m	1.400
Tower diameter	m	0.075
Tower base offset from ground	m	0.730

170 its fundamental mechanisms before turbulence and wake recovery dominate at larger spacings. Based on our measurements across $3-5D$, we assume that, at greater distances, motion-induced effects on power and loading of a downstream turbine will progressively diminish as coherent velocity structures generated by the upstream rotor dissipate due to turbulence development and wake mixing with the free stream. However, under very low inflow turbulence, which can keep the wake more stable and delay the decay of coherent flow structures, such effects may still remain measurable.

175 For the $3D$ and $5D$ configurations, WT2 was also shifted laterally in the negative y -direction by either $1R$ or $1D$, where R is the rotor radius. When offset by $1R$, approximately half of WT2 rotor is immersed in the wake of WT1; with a $1D$ offset, most of the rotor operates in free-stream flow, with only a small portion affected by the wake.

2.1.1 Wind turbine measurements

The WT1 platform position was measured using Wenglor PNBC107 laser transducers. The rotor forces of both wind turbines were measured using six-component ATI Mini45 force transducers (SI-580-20 calibration), mounted at the top of each tower. For WT1, the recorded loads include not only the aerodynamic forces generated by the rotor but also the inertial and gravitational loads of the rotor-nacelle assembly due to its motion. These non-aerodynamic contributions were removed following the method described by Fontanella et al. (2022a), allowing isolation of the pure aerodynamic loads. To isolate aerodynamic loads under platform motion, we adopt a two-test subtraction procedure. For each motion case, we run two tests with identical prescribed platform motion, but: (i) no-wind, rotor-locked test and (ii) wind-on, rotor-spinning test. The six-component tower-top signals from both tests are windowed to include the same integer number of motion periods and then subtracted (wind-on minus no-wind). This removes inertial and gravitational contributions of the rotor-nacelle assembly associated with the rigid-body motion, under the assumption that the model response is effectively rigid and equal in both tests. All aerodynamic forces are then expressed in the respective hub reference frames: $x_1-y_1-z_1$ $x_2-y_2-z_2$ for WT1 and

190 ~~$x_2 - y_2 - z_2$~~ ~~$x_2 - y_2 - z_2$~~ for WT2. The resulting signals contain approximately 100 full cycles of platform motion, ensuring a robust characterization of the quasi-periodic aerodynamic response.

2.1.2 Wake velocity measurements

Wake velocities reported in this paper refer to hot-wire measurements. Measurements of the streamwise velocity in the turbine wake were performed in a prior experimental campaign using a single hot-wire anemometer capable of measuring both mean
195 and fluctuating components of one-dimensional flow (Fontanella et al., 2025b). The probe was mounted on an automated traversing system, enabling measurements in the crosswind ($y_i - z_i$) plane. Velocity data were collected at $x_i = 3D, 4D$, and $5D$ downstream of the rotor, along horizontal (y_i -axis) and vertical (z_i -axis) lines centered on the hub. Spatial velocity fields were reconstructed by phase-aligning the measurements with the platform motion signal.

2.2 Wind turbine operating settings

200 All the main tests were carried out for a constant free-stream wind speed (U) of 4.0 ms^{-1} , which corresponds to a chord-based Reynolds number of approximately 1×10^5 at blade mid-span. The free-stream wind speed was measured by a Pitot tube positioned $3.13D$ ahead of the wind turbine on the hub axis. An additional measurement at 2.4 ms^{-1} was also performed and is discussed later in the paper. The free-stream flow was approximately uniform across the wind tunnel test section, as demonstrated in a previous study (Fontanella et al., 2025b). ~~The~~ the mean velocity over the WT1 rotor area varied by 5%
205 compared to the hub mean velocity, and the average turbulence intensity across the rotor disk was 1.5%. Large-eddy simulations of Pagamonci et al. (2025) showed that this relatively low free-stream turbulence contributes significantly to dissipating the coherent flow structures generated by platform motion, limiting the gains in wake recovery compared to the laminar-inflow case, where such gains are higher.

Another Pitot system was placed laterally to WT1 at $x_i = 0.8D$, $y_i = 2.1D$, and $z_i = 1.3D$ to measure the wind speed
210 influenced by blockage effects induced by the WT1 rotor, recording a wind speed of 4.2 ms^{-1} . The increase in wind speed due to wind tunnel blockage is sufficiently small, and multi-fidelity simulations by Bergua et al. (2023) on the wind turbine used in this study showed that blockage does not significantly alter its aerodynamic behavior. The effect can be accurately introduced in simulations by applying a corrected inflow velocity that reflects the value measured by the lateral Pitot system.

During testing, the air density (ρ) was 1.187 kgm^{-3} .

215 WT1 had a fixed rotor speed of 240 rpm and a collective blade pitch set to the optimal value of 0° . The turbine operated near its rated condition, which corresponds to the peak of the thrust curve under the standard pitch-to-feather control strategy, and therefore produced the strongest wake deficit. In these conditions the thrust coefficient (calculated by Eq. 6) was $C_t = 0.9$. Because rotor speed was held fixed at 240 rpm, the tip-speed ratio (TSR) varied with the apparent wind created by platform motion. Under the tested conditions, the TSR oscillation amplitude was 5% of its value observed in the bottom-fixed scenario.
220 This small modulation causes a slight dynamic shift of the operating point, without causing the rotor to enter a substantially different aerodynamic regime (the angle of attack varies by approximately $\pm 1^\circ$ at 70% of the rotor radius, as shown by Fontanella et al. (2021)).

The uniformity of the inflow generated by the wind tunnel across the region occupied by the wind farm was verified by measuring the loads on WT2 positioned at $5D$ downstream, under free-stream conditions with WT1 removed from the test chamber. This verification also ensured that WT2, when placed in the most downwind position, was not influenced by boundary effects near the end of the test section. Measurements were conducted at two wind speeds: 4.0 ms^{-1} and 2.4 ms^{-1} . The latter corresponds to the average wind speed over the rotor plane in the $5D$ full-wake condition, as estimated from the wake measurements reported by Fontanella et al. (2025b). At ~~2.4 ms^{-1}~~ , the rotor speed was set to ~~150 to maintain the optimal TSR~~ 150 rpm, corresponding to a TSR close to the optimal value of 7.5. The resulting deviation from the ideal TSR (about 4%) is due to the practical resolution with which the rotor speed can be prescribed and has a negligible effect on the operating conditions.

The energy available to WT2 when operating in non-free-stream conditions is reduced due to wake losses, which depend on its position relative to the upstream turbine. When outside of free-stream conditions, WT2 operated in a non-uniform wind field due to partial or total immersion in the wake of WT1, depending on its position. The operating conditions of WT2 were defined in terms of rotor-effective wind speed (U_{RE}), which at each location with fixed WT1 was obtained by inverting the calibrated thrust–wind speed–rotor speed relation derived by a blade-element momentum model of the rotor in free-stream conditions (see Appendix B). The rotor-effective wind speed is not intended as a reconstruction of the heterogeneous waked inflow; instead, U_{RE} denotes the speed of a uniform inflow that would generate the same mean thrust on the rotor. Since WT2 operates in open loop with a prescribed rotor speed, the rotational velocity does not characterize the inflow, and U_{RE} is therefore used as a metric to define a consistent operating point across different wake conditions.

The blade pitch of WT2 was fixed at 0° , as for WT1, and was not adjusted based on U_{RE} in order to avoid added complexity and to better isolate the effects of the wake on aerodynamic loading. The optimal TSR of the rotor (equal to 7.5), derived from the aerodynamic design, was used as the target operating condition. WT2 rotor speed was adjusted to achieve this optimal TSR based on the mean U_{RE} at each position, except in the 3D1D and 5D1D configurations. In these two cases, the U_{RE} for WT2 is higher than both the free-stream wind speed and the wind speed measured by the lateral Pitot system, which accounts for the blockage effect of WT1. The additional increase in velocity observed at WT2 is attributed to the local blockage caused by the WT2 rotor itself. In the 3D1D and 5D1D cases, the rotor speed was instead set to maintain the same thrust force as in the free-stream condition. As a result, the TSR was lower than the design value of 7.5 because of the blockage-induced speed-up at the rotor, but this choice ensured comparable thrust loading across the farm configurations. For the cases with dynamic WT1 motion, the rotor speed of WT2 was not updated instantaneously with the fluctuating inflow but kept constant at the value corresponding to the mean U_{RE} , so that WT2 experienced small deviations from the nominal TSR during the motion cycle. The resulting rotor speed values, fixed for each configuration, are specified in Table 2. For completeness and to support reproducibility, the table also reports the corresponding average thrust force and thrust coefficient of WT2, with C_t being computed according to Eq. 6 using the measured thrust and the reference free-stream velocity (constant during the tests at 4.0 ms^{-1}).

Table 2. Rotor effective wind speed (U_{RE}) and rotor speed, thrust (F_x), and thrust coefficient (C_t) of the downstream wind turbine in the different wind farm configurations tested in the experiment.

Configuration	U_{RE} [m/s]	Rotor speed [rpm]	F_x [N]	C_t [-]
3D	2.1	130	9.4	0.2
3D1R	3.3	190	22.0	0.5
3D1D	4.5	220	35.4	0.8
4D	2.3	140	10.9	0.3
5D	2.4	150	12.4	0.3
5D1R	3.3	190	23.7	0.6
5D1D	4.5	230	36.3	0.9

2.3 Platform motion scenarios

The experiment included both ~~unidirectional sinusoidal motions~~ sinusoidal platform motions, applied either in a single degree of freedom or as combined surge–sway motions, and realistic platform motions representative of a 10 MW floating wind turbine subjected to irregular wave excitation.

260 Platform motions were defined using the inertial reference frame ($x_i - y_i - z_i$) and the platform reference frame ($x_p - y_p - z_p$) that are depicted in Fig. 1b. The platform reference frame is fixed to the robotic platform and moves with the turbine; it has the origin O_p in correspondence of the tower base, on the tower centerline. z_p points along the tower axis, x_p points in the downwind direction when the platform is fixed and y_p forms a right-hand backhoe with x_p and z_p . The origin of the inertial reference frame O_i is at a vertical distance of 0.73 m from the ground. When the wind turbine is in the fixed position O_p is
265 coincident with O_i .

2.3.1 Sinusoidal motion

The system was studied under sinusoidal motion of different frequencies and amplitudes. For translational motions, the displacement was defined as

$$d(t) = a_m \sin(2\pi f_m t), \quad (1)$$

270 where a_m is the displacement amplitude and f_m the motion frequency. Surge motion corresponds to a translation of the platform reference point O_p along the x_i -axis. Surge–sway motion corresponds to a translation at an angle γ relative to the x_i -axis (and hence to the wind). The displacement components are $d_x(t) = d(t) \cos \gamma$ along the surge direction and $d_y(t) = d(t) \sin \gamma$ in the crosswind (sway) direction. Angles $\gamma = 15^\circ, 30^\circ, 45^\circ$, and 90° were tested.

For rotational motions, the platform angle was defined as

$$275 \theta(t) = a_\theta \sin(2\pi f_m t), \quad (2)$$

where a_θ is the angular amplitude. Pitch motion corresponds to a rotation around the y_1 -axis with the rotor hub located at a distance r_{hub} from the platform rotation point O_p . When θ is small, the resulting hub displacement along the wind direction is $d_{\text{hub},x}(t) = r_{\text{hub}}\theta(t)$. Yaw motion corresponds to a rotation around the z_1 -axis (see Fig. 1b).

Surge and pitch motions cause along-wind movement of the nacelle and result in an apparent wind speed over the rotor given
 280 by

$$u_a(t) = U - \dot{d}_{\text{hub},x}(t), \quad (3)$$

where $\dot{d}_{\text{hub},x} = \dot{d}$ in the case of surge motion, $\dot{d}_{\text{hub},x} = \dot{d}\cos\gamma$ in the case of surge-sway motion, and $\dot{d}_{\text{hub},x} = r_{\text{hub}}\dot{\theta}$ in the case of pitch motion. Accordingly, the amplitude of the apparent wind oscillation is $\Delta u = 2\pi f_m a_m$ in the case of surge motion, $\Delta u = 2\pi f_m a_m \cos\gamma$ in the case of surge-sway motion, and $\Delta u = 2\pi f_m r_{\text{hub}} a_\theta$ in the case of pitch motion.

285 During yaw motion, because the yaw amplitude is small, the apparent velocity remains predominantly aligned with the x_1 -axis. However, a velocity gradient develops across the rotor span: the apparent wind speed perturbation is largest at the blade tips and vanishes at the hub. The local apparent velocity at a position p_y along the y_p -axis (measured from the hub, with sign) is

$$u_a(t, p_y) = U - \dot{\theta}(t)p_y, \quad (4)$$

290 The oscillation amplitude of the apparent velocity therefore scales linearly with spanwise position, $\Delta u(p_y) = 2\pi f_m a_\theta p_y$.

In research concerning the unsteady aerodynamics of floating wind turbines (Fontanella et al., 2021; Messmer et al., 2024a; Schulz et al., 2024), frequencies are typically expressed in a non-dimensional form using the rotor reduced frequency (f_r), which is equivalent to a Strouhal number and is defined as:

$$f_r = \frac{f_m D}{U}. \quad (5)$$

295 The sinusoidal motion conditions were characterized in terms of reduced frequency and amplitude. The selected amplitudes and frequencies were based on those used in the previous wind tunnel experiment of Fontanella et al. (2025b) that characterized the wake behavior. The selected conditions were known to cause significant dynamic variations in the wake and were consequently expected to produce a substantial aerodynamic excitation of the downstream turbine. The frequencies correspond to reduced frequency values representative of full-scale floating wind turbine dynamics. Specifically, at a wind speed of 12 ms^{-1} ,
 300 $f_r = 0.3$ and $f_r = 0.6$ correspond to full-scale frequencies of 0.02 Hz and 0.04 Hz, respectively, which are typical of rigid-body modes in 10 MW floating turbines. In contrast, $f_r = 1.2$ corresponds to a full-scale frequency of 0.08 Hz (with a period of 12.5 s), representative of platform motions at wave frequency.

The amplitudes of surge and pitch motions caused an apparent wind speed variation, expressed as a ratio of apparent wind to undisturbed wind speed ($\Delta u/U$), of approximately 5% at all reduced frequency values considered in the experiment. In
 305 surge-sway motion, the displacement amplitude d was the same as in pure surge, but the variation in apparent wind speed decreased as the angle between the motion direction and the wind (γ) increased. For yaw motion, an amplitude of 2° was selected, to investigate wake development under large dynamic yaw rotations, representative of those that may occur in real

operating conditions under severe sea states. When combined with reduced frequencies of 0.3, 0.6, and 1.2, this yaw motion amplitude resulted in apparent wind speed variations at the rotor edge of approximately 3%, 7%, and 13%, respectively.

310 2.3.2 Irregular waves

Following the analysis of cases with sinusoidal motions, the experiment was extended to include motions similar to those induced by irregular waves acting on a 10 MW floating wind turbine from different directions, in order to assess whether the observations from the simplified cases remained valid under more realistic conditions.

In these tests, unlike the sinusoidal cases, the wind turbine motion was not prescribed from simple parametric inputs but was
 315 obtained from aero-hydro-servo-elastic simulations of a realistic floating wind turbine. Specifically, we modelled the SOFTWIND system, which consists of the DTU 10 MW wind turbine mounted on a spar-buoy platform (Arnal, 2020; Behrens de Luna et al., 2024; Papi et al., 2024), using the OpenFAST simulation tool (Jonkman et al., 2023). Table 3 reports the frequencies of the rigid-body motion modes of the SOFTWIND floating wind turbine. At these frequencies, the platform motion exhibits significant amplification of the excitation from wind and wave forcing.

Table 3. Frequencies of the rigid-body motion modes of the SOFTWIND floating wind turbine, with reduced frequencies evaluated at a mean wind speed of 12 ms^{-1} .

Mode	Frequency (full scale) [Hz]	Frequency (model scale) [Hz]	Reduced frequency (f_r)
Surge and sway	0.008	0.208	0.12
Roll and pitch	0.031	0.780	0.47
Yaw	0.077	1.925	1.16

320 The OpenFAST simulations were run for representative wind and wave conditions, and the resulting platform motion time series were used as inputs to the wind-tunnel experiments. The waves in the simulation had a full-scale significant height of 5 m and a peak period of 12 s corresponding to a model-scale significant height of 0.067 m and a peak period of 0.48 s. The same waves were applied at heading angles of 0° and 30° relative to the wind direction. The simulations were carried out with a uniform wind field with a full-scale wind speed of 12 ms^{-1} and turbulence intensity of 1.5%, fixed rotor speed and blade
 325 pitch, matching the conditions of the experiment. The time series of platform motions in six directions were downscaled and employed to prescribe the motion of WT1 utilizing the robotic platform.

The time series of platform motions induced by irregular waves are shown in Fig. 2 and the corresponding spectra in Fig. 3. When waves are aligned with the wind direction (0°), the platform response is dominated by surge and pitch, with minimal motion in the other degrees of freedom. In contrast, waves at 30° also excite significant sway, roll, and yaw movements.
 330 Figure 2 shows that the frequency and amplitude of the platform motions of the SOFTWIND driven by the selected wave conditions are similar to those in the sinusoidal motion cases. Specifically, sinusoidal surge–sway and yaw motions represent movements in the sway and yaw directions caused by waves with a 30° heading.

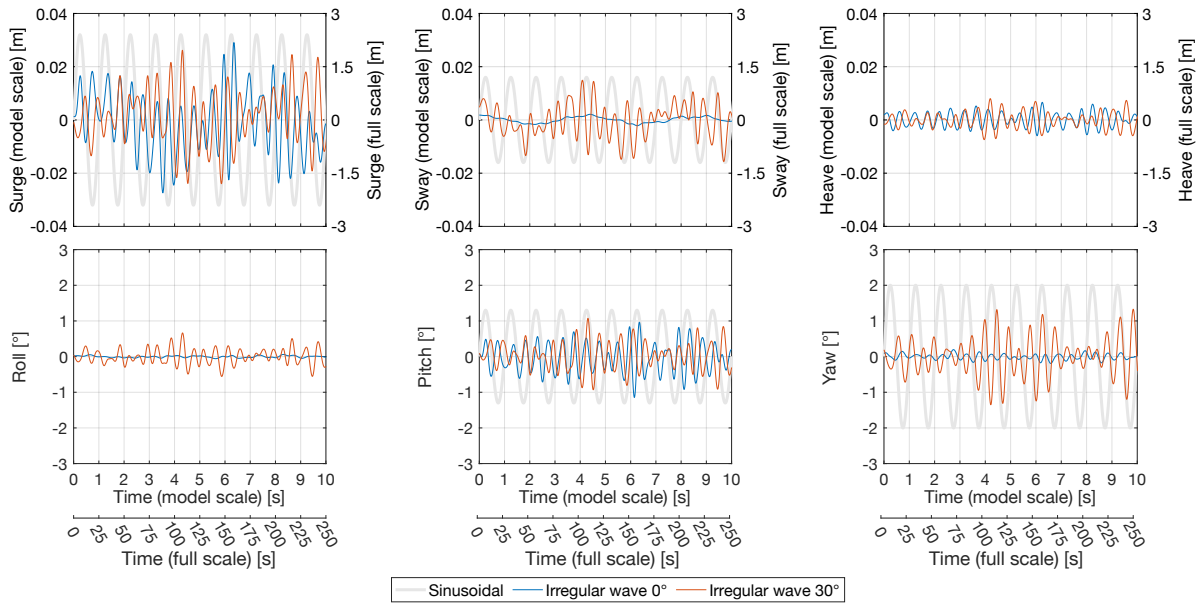


Figure 2. The time series of wave-induced motions examined in the experiment are compared with sinusoidal motions of $f_T = 0.6$. The wave-induced motions correspond to the SOFTWIND 10 MW floating wind turbine subjected to irregular waves with a significant height of 5 m and a peak period of 12 s (full scale).

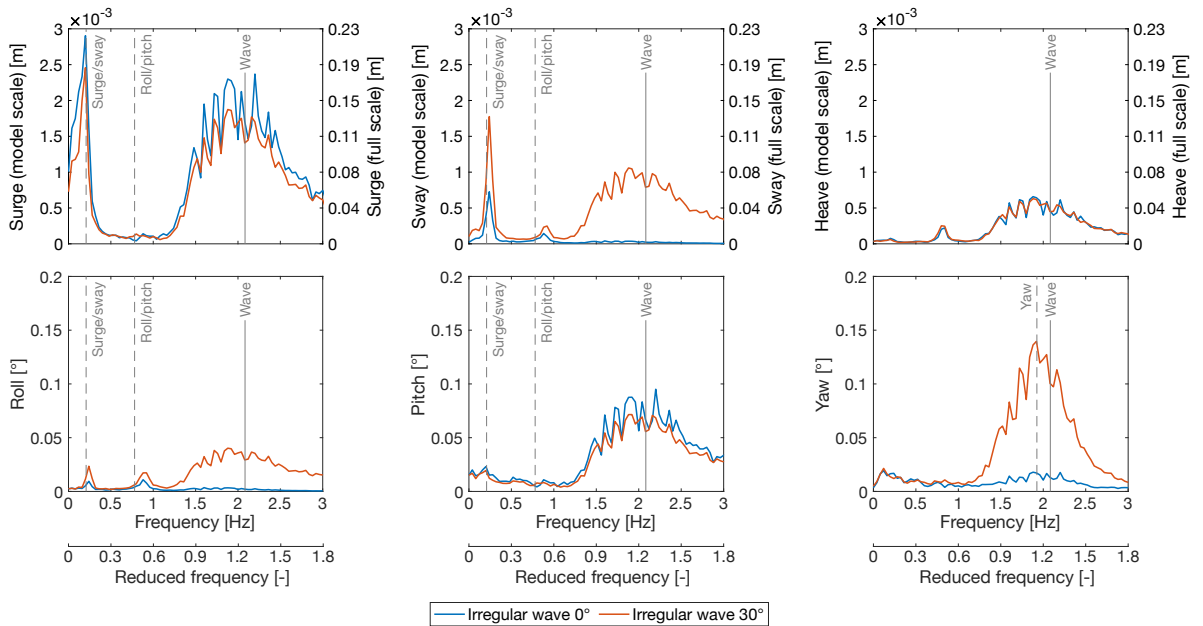


Figure 3. Spectra of wave-induced motions of the SOFTWIND 10 MW floating wind turbine subjected to irregular waves with a significant height of 5 m and a peak period of 12 s (full scale).

3 Results

The experimental campaign produced an extensive dataset, which is openly available (Fontanella et al., 2025a). This paper
335 focuses on a subset of cases selected for their relevance to floating wind farm dynamics and for the insights they offer into the
effects of platform motion and array configuration on wake interactions.

The analysis of the results uses the aerodynamic thrust force (F_x) and the torque (M_x) as key indicators of rotor performance.
Thrust plays a critical role in the coupled dynamics of floating wind turbines, linking aerodynamic forces to platform motion
and contributing significantly to tower and blade loading. Torque, on the other hand, governs power generation and influences
340 drivetrain dynamics. In the experiment, the wind turbines operated at a fixed rotor speed, so the aerodynamic power was directly
calculated as the product of aerodynamic torque and rotor speed.

To enable comparison with other studies, rotor loads are also reported in terms of non-dimensional coefficients. The thrust
coefficient is defined as

$$C_t = \frac{F_x}{\frac{1}{2}\rho\pi R^2 U^2}, \quad (6)$$

345 and the torque coefficient as

$$C_q = \frac{M_x}{\frac{1}{2}\rho\pi R^3 U^2}, \quad (7)$$

where U is the reference wind speed measured with the Pitot tube placed upstream of the rotor along the hub axis. During the
tests this velocity remained constant at 4.0 ms^{-1} . In this study, the same free-stream velocity U is used for the normalization of
both WT1 and WT2 loads. This convention is often adopted in wake and wind farm studies (e.g., by Van Der Hoek et al. (2024)),
350 as it facilitates direct comparison of upstream and downstream turbine performance under identical reference conditions.

No blockage correction was applied to the results reported in this paper. Classical correction methods (Inghels, 2013) are
based on simplified one-dimensional flow assumptions and are valid only for isolated rotors in uniform inflow. While they
could be applied to WT1 operating in free stream, they cannot be consistently extended to WT2 when it is partially or fully
immersed in the wake of WT1. To ensure consistency across turbines and configurations, the results are therefore presented
355 without correction.

3.1 Time-average loads

This section presents an analysis of the average loads on the two wind turbines. Specifically, thrust and torque were evaluated
in the fixed-tower base configuration to assess the aerodynamic response of each turbine and the overall wind farm behavior
across different layouts (Sect. 3.1.1). The time-average power output was examined under prescribed motions of the upstream
360 turbine to quantify the impact of platform motion on wake recovery (Sect. 3.1.2).

3.1.1 Fixed tower base

The loads of WT1 in the fixed-tower base condition were measured in 40 repeated test runs. These repetitions were carried
out throughout the experimental campaign, particularly after any changes in the test setup and following system initialization,

for example at the beginning of each testing day, to ensure consistency of the measurements. The average thrust force was 36.17 N and the average torque was 2.87 Nm. The loads were consistent during the experimental campaign, with maximum deviations from their mean values of ± 0.33 N for thrust and ± 0.1 Nm for torque. Under these conditions, WT1 produced an average power of 72 W, corresponding to a full-scale value of 10.93 MW.

To verify the aerodynamic equivalence of WT2 with respect to WT1, WT2 was mounted on the robotic platform in WT1 position, and its performance was compared under identical operating conditions. The measured thrust force (35.9 N) and torque (3.03 Nm) for WT2 fell within the range recorded for WT1, confirming that WT2 rotor had equivalent aerodynamic performance.

The average WT2 loads are shown in Fig 4. When WT2 operated in free-stream conditions at the 5D position (with WT1 removed) and a wind speed of 4.0 ms^{-1} , its loads were consistent with those measured when the turbine was mounted on the robotic platform. At a wind speed of 2.4 ms^{-1} , which is representative of the average velocity in full-wake conditions, the thrust force of WT2 matched the scaled thrust of the DTU 10 MW turbine used as the reference in rotor design. These results confirm that the wind tunnel provided a uniform inflow across the wind farm region and that the aerodynamic response and induction of the downstream turbine ~~was~~ were not significantly influenced by proximity to the end of the test section. This comparison is not intended to reproduce waked inflow conditions, but simply to verify that, in the absence of a wake, WT2 operates consistently at a downstream spacing of $5D$ as it does at the other tested spacings.

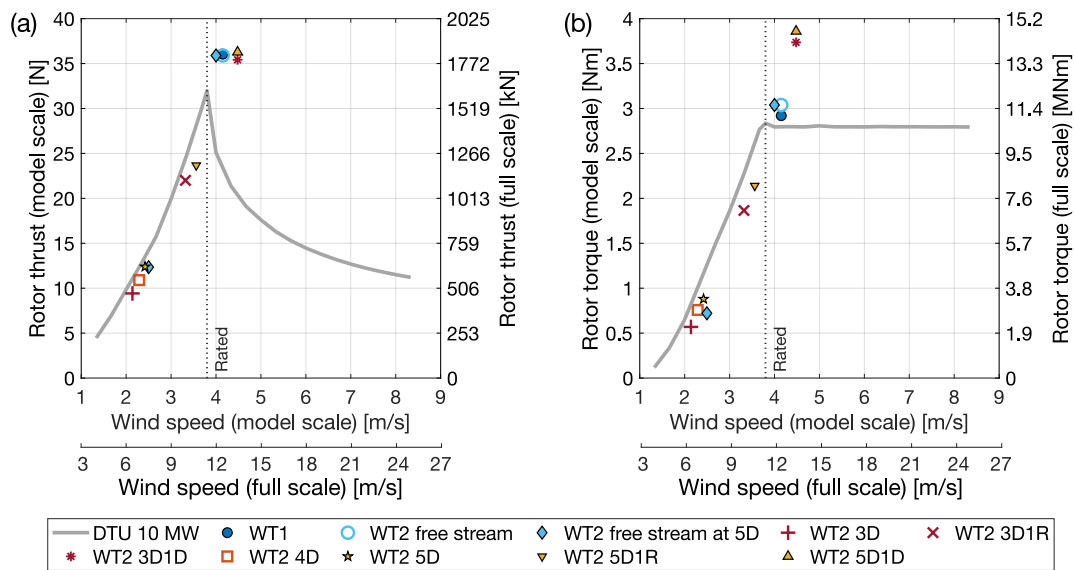


Figure 4. Rotor thrust (a) and rotor torque (b) of the two wind turbines in the scenario without platform motion and for different positions of WT2 with respect to WT1. The loads of WT1 and of WT2 in the free stream condition are plotted against the wind speed measured by the Pitot system, while the loads of WT2 in all other configurations are plotted against the estimated rotor-effective wind speed.

380 WT2 loads in farm scenarios with fixed WT1 were recorded across all farm configurations, with 2 to 9 repeated tests. In
the configurations with aligned turbines and those with a lateral offset of $1R$ the U_{RE} for WT2 is below the rated wind speed
and the loads follow adequately the values of the DTU 10 MW at model scale. In configurations with a lateral offset of $1D$,
the effective wind speed U_{RE} for WT2 exceeds the rated wind speed, resulting in a TSR lower than the optimal value for the
rotor. While the thrust remains equal to that of the turbine in free-stream conditions, as intended when defining the operating
385 parameters, the torque is higher.

3.1.2 ~~Impact~~ Effect of platform motion on energy recovery the time-averaged power of the downstream turbine

Large rotor motions induced by platform dynamics introduce dynamic variations in aerodynamic loads, which in turn alter
the wake dynamics. This disturbance might enhance the natural mixing between the wake and the surrounding free stream,
leading to earlier wake recovery compared to a case where the turbine is fixed at the tower base. Earlier mixing implies that the
390 flow regains free-stream characteristics closer to the rotor, thereby increasing the available energy for a downstream turbine.
Wake velocity measurements obtained from hot-wire anemometry at the WT2 positions by Fontanella et al. (2025b) showed
only minor increases in mean wind speed relative to the fixed case. Larger improvements were observed in crosswind and yaw
motion cases, with more significant gains at $5D$.

To ~~directly assess the impact of motion of the upstream rotor on~~ assess the influence of upstream rotor motion on wake
395 energy recovery, we measured the power output of WT2 ~~placed at various at several downstream~~ positions in the wake of WT1.
Because the rotor speed was prescribed and constant in each farm configuration, the aerodynamic power of both turbines was
obtained directly from the measured torque and the known rotational speed. In all tests, WT1 maintained a time-average power
output of 72 W (10.93 MW at full scale). Figure 5 shows the ratio of WT2 power to WT1 power for various farm configurations
and WT1 motion conditions, including the fixed-tower base ~~reference case.~~ The complete set of time-averaged power
400 measurements for every farm configuration, including all amplitudes and frequencies tested for sinusoidal motions, is provided
in Appendix C. For sinusoidal platform motions, the ~~reported values represent values reported in Figure 5 correspond, for each~~
farm configuration, to the maximum WT2 power observed across all tested combinations of frequency and amplitude for ~~each~~
that motion type.

When WT2 is fully aligned with WT1, it operates in the core of the wake and generates the lowest power. In the fixed case,
405 WT2 power increases modestly from 11% to 18% of WT1 power as the distance between the turbines increases from $3D$ to
 $5D$, reflecting gradual wake recovery. These wake losses are larger than those typically observed in full-scale studies, where
the power of downstream turbines at $5D$ often is often 40–50% of the power of the upstream turbine (Shen and Mikkelsen,
2011). In our experiments, the stronger losses arise from the combination of the high thrust coefficient of WT1 (average
 $C_t = 0.9$) and the very low inflow turbulence intensity (1.5%), which limit wake recovery. The value of C_t is consistent with the
410 operating conditions reported in previous wind tunnel experiments on floating wind turbine aerodynamics, where model rotors
were typically operated near rated conditions and produced similarly high thrust coefficient (Fontanella et al., 2021, 2022a,
2025b). In these conditions, the wake deficit is highly persistent, leading to a stronger impact on the downstream turbine. As

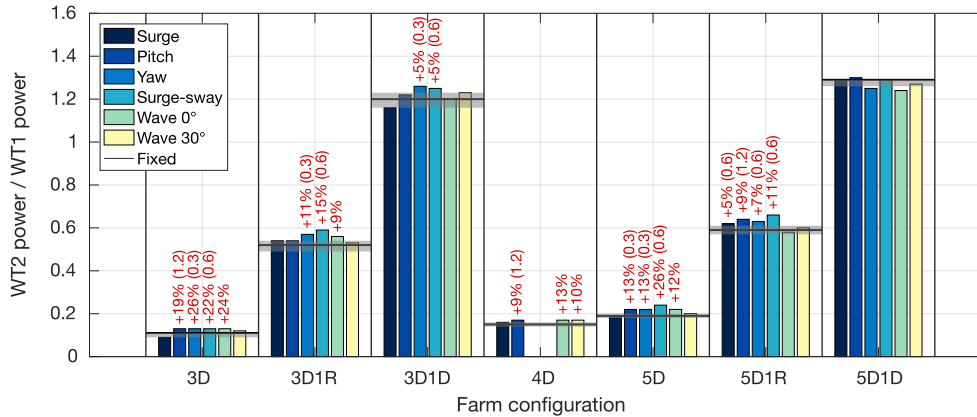


Figure 5. Maximum time-averaged Time-averaged power output of WT2, normalized by that of WT1, for various WT1 motion scenarios. For sinusoidal platform motions, the values shown correspond, for each farm configuration, to the maximum WT2 power observed among all tested combinations of WT1 frequency and amplitude for that motion type. The shaded area shows bands indicate the variability (minimum/maximum) of WT2 power variability in fixed-fixed-turbine conditions. Percentages above the bars indicate improvements over denote the relative improvement with respect to the fixed case when they exceed this exceeds the variability, while the values in parentheses denote indicate the reduced frequencies-frequency of the sinusoidal motions-motion at which these gains were observed the maximum gain occurred.

a result, variations in the wake deficit caused by upstream turbine motion have a pronounced effect on the performance of the downstream turbine, whereas under weaker wake interactions such variations would play a minor role.

415 As expected, the power generated by WT2 improves with lateral offset from the wake centerline. At an offset of $1R$, WT2 produces approximately 55% of WT1 power, as the rotor becomes only partially immersed in the wake. When the offset reaches $1D$, WT2 actually generates more power than WT1, consistent with the overspeed observed in the estimates of rotor-averaged wind speed.

When WT1 undergoes platform motion, WT2 power increases under certain motion types relative to the fixed case. The 420 most significant power gains were observed with sinusoidal yaw and surge-sway motions at reduced frequencies of 0.3 and 0.6. Wake velocity measurements reported by Fontanella et al. (2025b) indicate that these motion types have the strongest impact on wake recovery. Motions driven by stochastic wave excitation at 0° incidence led to power gains comparable to those observed under sinusoidal pitch motion. For instance, in the 3D configuration, sinusoidal pitch motion resulted in a 2619% increase in WT2 power, while wave-induced motion at 0° , which excited platform pitch, produced a similar gain of 24%. In 425 contrast, wave excitation at 30° incidence, which introduced significant crosswind and yaw motions, did not lead to increased power output for WT2. This differs from the sinusoidal motion cases, where crosswind and yaw motions were generally associated with noticeable power gains.

While relative power gains are most pronounced when WT2 is fully aligned with WT1, they remain small in absolute terms due to the inherently low baseline power in this configuration. The highest relative power increases over the fixed-turbine

430 case (+26%) were observed in two scenarios: the 3D aligned configuration with WT1 undergoing yaw motion (2° amplitude, reduced frequency 0.3), and the 5D aligned configuration with WT1 undergoing sway motion of 0.032 m amplitude (2.4 m at full scale), perpendicular at a $\gamma = 45^\circ$ angle with respect to the wind ($\gamma = 90^\circ$), with reduced frequency 0.30.6. In the 3D yaw case, WT2 power increased from 11% to 13% of WT1 power, corresponding to a rise from 7.7 W (1.17 MW at full scale) to 9.7 W (1.47 MW), ~~while WT1 maintained a constant output of 72 (10.93)~~. In the 5D surge-sway case, WT2 power increased
435 from 19% to 24% of WT1 power, rising from 13.8 W (2.1 MW at full scale) to 17.4 W (2.64 MW).

While relative gains are most pronounced in aligned configurations, the absolute power increases are more substantial in partially misaligned layouts. For instance, in the 3D1R configuration, when WT1 underwent surge-sway motion at a reduced frequency of 0.6 with an amplitude of 0.032 m (equivalent to 2.4 m at full scale) and oriented at a $\gamma = 45^\circ$ angle to the wind, the power output of WT2 increased from 52% to 59% of WT1 power. In absolute terms, this corresponds to a rise from 37.1 W
440 (5.63 MW at full scale) to 42.5 W (6.45 MW at full scale). Conversely, when WT2 was laterally offset by a full rotor diameter ($1D$), the influence of WT1 motion on downstream power became negligible.

3.2 Dynamic loads from upstream turbine movement

In addition to promoting wake mixing, the disturbances introduced by rotor motions can propagate downstream and induce dynamic loading on other turbines in the wind farm.

445 Figure 6 shows the aerodynamic thrust and torque measured on WT1 and WT2 when WT1 undergoes surge and pitch motions at a reduced frequency of 0.6 and with $\Delta u/U$ of 5%; in these tests, the two turbines are aligned and spaced $3D$ apart. Surge and pitch motions are considered because they both involve nacelle translation in the wind direction, directly altering the apparent wind speed at the rotor, and are therefore expected to produce similar effects on the aerodynamic loads. In the figure, the load time series were binned and phase-averaged according to WT1 platform motion to show variations at the platform
450 motion frequency. The results are reported both in dimensional form (force and torque) and as non-dimensional coefficients. The thrust and torque coefficients were computed using Eq. 6 and Eq. 7, with the free-stream velocity U measured by the Pitot tube located upstream of WT1 on the hub axis (constant during the tests at 4.0 ms^{-1}).

In both cases, the thrust and torque of WT1 exhibits a clear sinusoidal variation at the same frequency as the platform motion. The peak loads occur at half the motion period, when the nacelle reaches its maximum upstream velocity. This behavior, well
455 documented in previous experimental and numerical studies (Bergua et al., 2023), confirms that the loads oscillations are primarily driven by variations in apparent wind due to platform motion. The rotor loads follow these variations proportionally, indicating a quasi-steady response.

The pulsating loads on WT1 generate a periodically varying momentum deficit and shed vorticity in the wake; additionally, the rotor itself moves in space during the platform motion cycle. Together, these effects create flow structures that evolve
460 with the same periodicity as the rotor motion and remain coherent with it as they are advected downstream. For surge and for small-amplitude pitch motion, these structures manifest as a pulsing of the wake velocity, with periodic acceleration and deceleration of the flow during the motion cycle (Fontanella et al., 2025b; Messmer et al., 2024a). This pulsing behavior is illustrated in Fig. 6, which shows the velocity in the wake of WT1 at $3D$ downstream, spatially averaged along a horizontal line

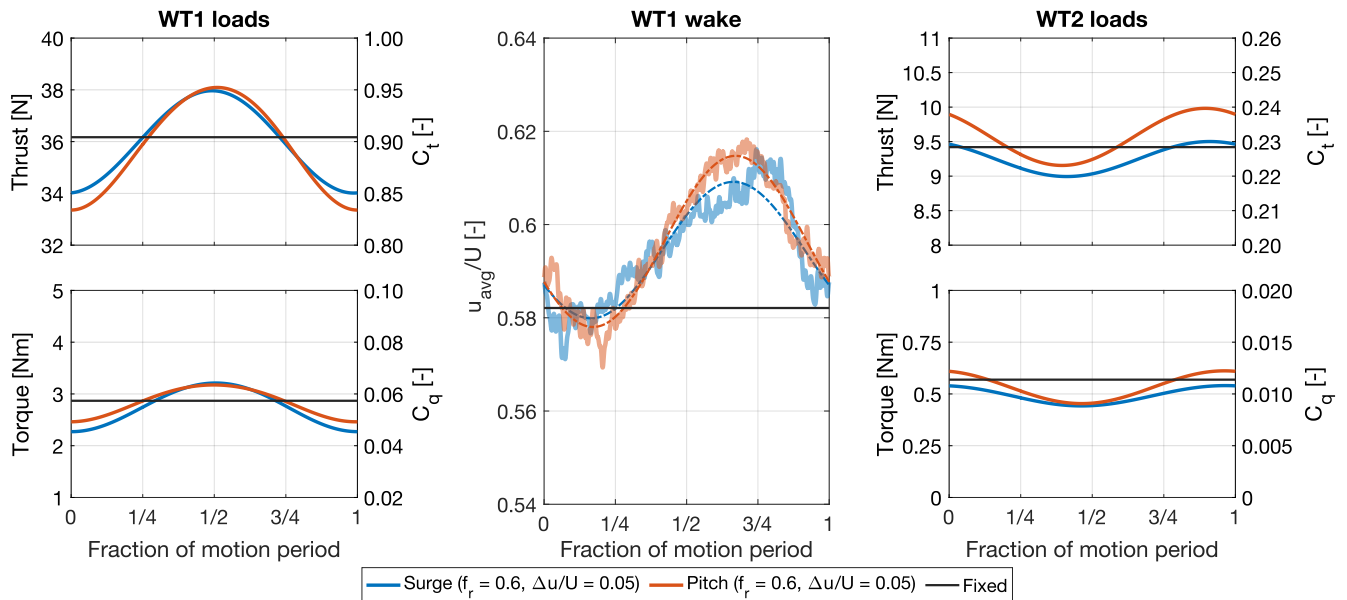


Figure 6. Rotor thrust and torque of WT1 and WT2, together with the spatially averaged wake velocity (u_{avg}) of WT1 along a horizontal line at hub height. WT2 is positioned $3D$ downstream of WT1, and the wake is evaluated at the same distance. Three cases are compared: WT1 undergoing surge motion ($f_r = 0.6$, $\Delta u/U = 5\%$), WT1 undergoing pitch motion ($f_r = 0.6$, $\Delta u/U = 5\%$), and WT1 fixed.

at hub height within the extent of the WT2 rotor ($-D < y < D$). Wake velocity data are obtained from hot-wire measurements
 465 reported in Fontanella et al. (2025b). Since velocity fluctuations are not uniform across the wake (see spectra of Fig. 9), this
 metric provides only a qualitative measure of the inflow over WT2 rotor. Nevertheless, both surge and pitch motions produce
 periodic increases and decreases of the spatially averaged velocity, with comparable amplitude ($\sim 1.5\%$ of U) and a phase shift
 relative to the platform motion.

The unsteady wake of WT1 therefore creates a periodically varying inflow for WT2. In response, WT2 exhibits periodic
 470 thrust and torque fluctuations at the same frequency as the motion of the upstream turbine. The amplitude of these oscillations
 is much smaller than for WT1: in the surge case, 0.25 N versus 1.98 N in thrust and 0.05 Nm versus 0.47 Nm in torque. The
 peaks in WT2 loads occur with a delay of about 0.4 motion periods relative to WT1 (i.e., a phase shift of $\sim -260^\circ$).

The reduced amplitude of WT2 load oscillations reflects the fact that the velocity fluctuations in the wake are weaker and
 more non-uniformly distributed across the rotor compared to the apparent-wind variations acting on WT1, which are generated
 475 by its own motion. At the reduced frequency of 0.6, the induction response of the scale-model rotor to such inflow variations is
 expected to be quasi-steady (Bergua et al., 2023; Schulz et al., 2024), as also evidenced by the WT1 loads when its own motion
 modulates the inflow. A similar quasi-steady behavior can therefore be assumed for WT2, meaning that induction dynamics do
 not introduce additional phase shifts or attenuate the load amplitude. The observed time lag is thus primarily associated with
 the advection of coherent flow structures shed by WT1.

480 Figure 7 presents the Fast Fourier Transform (FFT) of the thrust force of WT2 when aligned with WT1 and positioned at various downstream distances. In these tests, WT1 undergoes surge or pitch motions at reduced frequencies of 0.3, 0.6, and 1.2, with $\Delta u/U$ of 5%. The FFT is used to quantify load variations at the motion frequency and to identify whether additional harmonics appear at other frequencies.

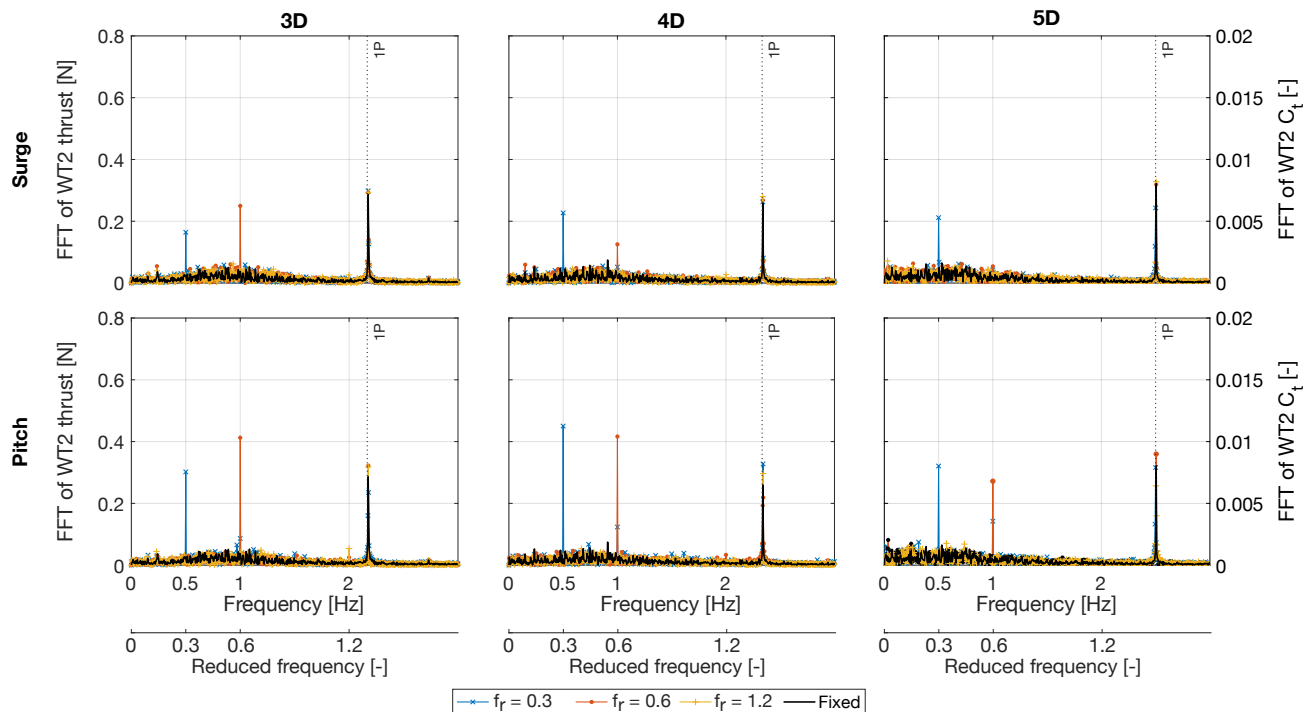


Figure 7. Fast Fourier Transform (FFT) of the thrust force on a downstream wind turbine operating in the wake of an upstream turbine subjected to sinusoidal surge and pitch motions with apparent wind-to-undisturbed wind speed ratios of 5%. The turbines are aligned, and the downstream turbine is placed at multiple distances downstream of the upstream rotor.

485 The load spectra of WT2 consistently show a sharp peak at the frequency of WT1 platform motion, corresponding to the periodic load oscillations observed in Fig. 6. Across all tested configurations, this spectral peak is clearly visible at the excitation frequency, while the rest of the spectrum remains largely unchanged relative to the fixed case. Figures 6 and 7 show that surge and pitch motions producing equal variations in apparent wind speed lead to dynamic loads of comparable amplitude on the downstream wind turbine. In general, load variations are slightly higher for pitch motion than for surge motion, likely due to the additional vertical wake meandering induced by pitch.

490 WT2 exhibits a clear dynamic response at the frequency of WT1 motion when the reduced frequency is 0.3 or 0.6, confirming that the upstream rotor motion is the primary driver of its load oscillations. This response is not observed at $f_r = 1.2$, indicating that higher-frequency motions of the upstream platform do not significantly influence the downstream turbine. This observation is consistent with the findings of Fontanella et al. (2025b), who reported that wake velocity oscillations induced by platform

495 motion decrease in strength as the reduced frequency increases from 0.6 to 1.2. At a reduced frequency of 1.2, the periodic velocity structures in the wake of WT1 at the WT2 location have reduced amplitude and rapidly become comparable to the background turbulence of a fixed-turbine wake.

At a reduced frequency of 0.6, the spectral peak in WT2 thrust is visible at distances of $3D$ and $4D$ from WT1 but disappears at $5D$. This again agrees with previous wake measurements of Fontanella et al. (2025b), which showed that at larger distances, turbulence in the flow masks the periodic structures introduced by platform motion. The observed reduction in motion-induced effects with increasing spacing is consistent with a gradual loss of wake coherence due to turbulence and shear-layer instabilities. As the wake advects downstream, motion-imposed velocity patterns are progressively replaced by smaller-scale turbulence, diminishing their influence on the downstream rotor.

500 Interestingly, when WT1 is subjected to pitch motion at a reduced frequency of 0.3, a secondary spectral peak appears at twice the excitation frequency. The amplitude of this second harmonic increases with the spacing between the turbines. This peak is absent under surge motion at the same reduced frequency, despite producing similar variations in apparent wind speed, and is of much lower magnitude in the other pitch cases with higher frequency and smaller rotation amplitude. This difference is attributed to the nature of pitch motion, which periodically tilts the rotor upward and downward, causing vertical deflection of the wake. As a result, the wake undergoes oscillatory vertical motion. The second harmonic in the WT2 load spectrum likely originates from this vertical displacement: each upward or downward shift of the wake produces a drop in thrust on WT2, creating a load fluctuation at twice the pitch motion frequency.

The effect is most evident at a reduced frequency of 0.3 because this case produces the largest rotor tilt amplitude (2.5°) and, consequently, the greatest vertical wake deflection. This interpretation is supported by Fig. 8, which shows phase-averaged velocity fields in the wake of the upstream turbine at $3D$, measured with hot-wire probes as reported in Fontanella et al. (2025b), for two pitch motions: reduced frequency 0.3 with 2.5° amplitude, and reduced frequency 0.6 with 1.3° amplitude. In both cases, the wake exhibits periodic acceleration and deceleration, but in the 2.5° case the upper portion of the wake also undergoes a clear periodic vertical displacement, consistent with the second harmonic present in the load spectrum of the downstream turbine.

3.2.1 Effect of turbine relative positioning

520 The influence of lateral offset between the two turbines on the dynamic loading induced by the wake of a moving upstream turbine on a downstream rotor is examined for a pitch motion with an amplitude of 1.3° and a reduced frequency of 0.6. This case was selected because the motion produces pronounced velocity oscillations in the wake of the upstream turbine (see Fig. 8) and induces clear dynamic loads on the rotor of the downstream turbine in aligned configurations.

525 Figure 9 presents the power spectral density (PSD) of the wake velocity at hub height, measured with hot-wire probes by Fontanella et al. (2025b), at different downstream locations. The figure also shows the amplitude of thrust and torque oscillations at the platform motion frequency experienced by the downstream turbine. In the figure, the thrust and torque amplitudes for the "Fixed" case represent the load oscillations experienced by WT2 when WT1 has fixed tower base. These values are extracted from the load spectra evaluated at a reduced frequency of 0.6, [by computing the FFT of the load signals](#)

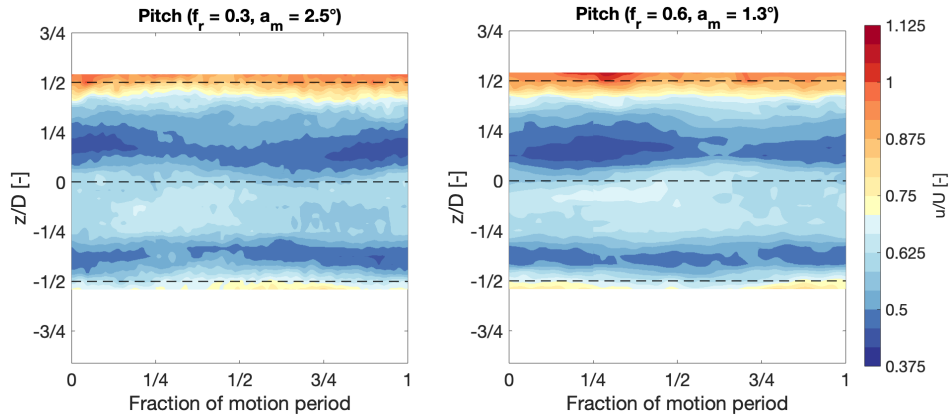


Figure 8. Phase-averaged velocity along the vertical line passing through the rotor axis of the upstream turbine wake at a downstream distance of three rotor diameters, for cases with pitch motion. The two motions have the same apparent wind-to-undisturbed-wind speed ratio of 5%, but differ in frequency and amplitude.

and taking the magnitude of the spectral component at that frequency. The observed oscillations in this configuration result from turbulence generated by the upstream turbine and the natural meandering of its wake.

530 In all farm configurations, WT2 experiences greater load amplitudes when WT1 is subject to platform motion than when it is fixed. The dynamic loads on WT2 reach their maximum when it is aligned with WT1. In this configuration, WT2 operates fully within the wake of WT1, and velocity fluctuations at the platform motion frequency affect the entire rotor-swept area. In the velocity PSD, the spectral peak corresponding to the motion frequency is less prominent at $5D$ than at closer distances, as it is masked by turbulence that increases downstream the rotor. As a result, the motion-induced loads on WT2 are also

535 reduced at $5D$, consistent with observations from Fig. 7. In the $4D$ configuration, the loads amplitude is maximum. This trend is consistent for both thrust and torque. The motion of WT1 induces zero-to-peak variations in WT2 thrust of 0.4 N (equivalent to 20.3 kN at full scale) representing approximately 3% of the average thrust developed by the turbine. The torque variation reaches 0.084 Nm (319.3 kNm at full scale), corresponding to about 12% of the turbine average torque.

As WT2 is laterally offset from WT1, the amplitude of its dynamic load oscillations decreases. This reduction occurs because

540 a larger portion of WT2 rotor operates outside the wake. With increasing offset, only part of the rotor is exposed to the unsteady wake flow, while the remainder encounters relatively steady free-stream conditions. The steadier inflow on part of the rotor mitigates the effects of the wake-induced fluctuations, leading to a net reduction in dynamic loading. When the offset reaches one rotor diameter, motion-induced loads on WT2 become negligible. This conclusion, however, is specific to the streamwise spacing investigated in this study ($3 - 5D$). At larger spacings, wake spreading would increase the fraction of the rotor exposed

545 to unsteady flow, potentially modifying this trend.

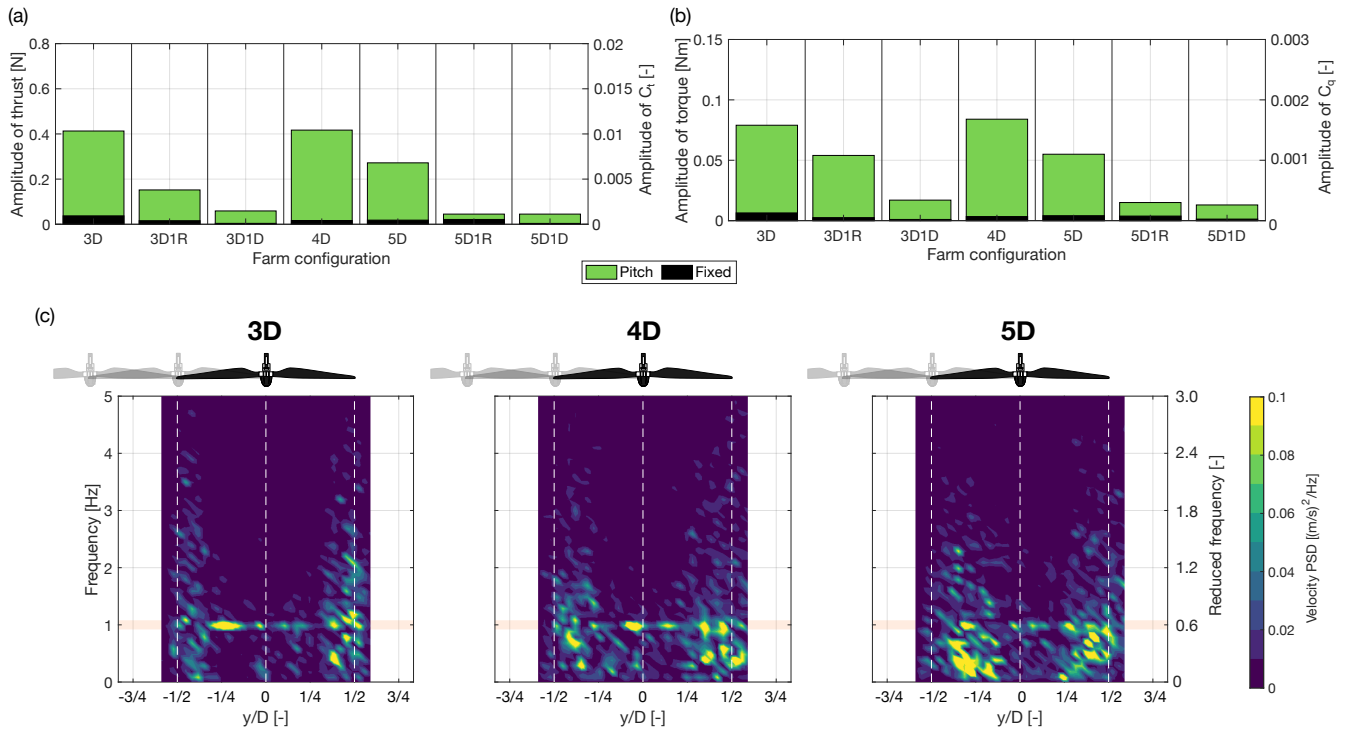


Figure 9. Effect of velocity oscillations induced by platform pitch motion with 1.3° amplitude and a reduced frequency 0.6 on the loads of a downstream wind turbine operating in the wake, at varying downstream distances and crosswind positions. **(a):** amplitude of thrust oscillations on the downstream turbine. **(b):** amplitude of torque oscillations on the downstream turbine. **(c):** power spectral density (PSD) of the velocity in the wake of the upstream turbine at different downstream locations.

3.2.2 Effect of motion-driven wake meandering

While surge and pitch motions primarily induce oscillations in thrust that lead to a pulsating wake, motions in the crosswind (sway) and yaw directions predominantly excite lateral meandering of the wake (Messmer et al., 2024a; Fontanella et al., 2025b) (Messmer et al., 2024a; Fontanella et al., 2025b; Messmer et al., 2025). Here, the term “meandering” refers to the coherent lateral displacement of the wake forced by the platform motion, which differs from the natural large-scale meandering that typically develops in the far wake of a bottom-fixed turbine. This side-to-side displacement of the wake introduces a different type of unsteadiness in the flow compared to the pulsing associated with surge and pitch. A rotor operating in such a wake is therefore subjected to dynamic loads that differ from those generated by along-wind motion of the upstream turbine. Section 3.2.3 investigates yaw motion, while Sect. 3.2.4 analyzes crosswind motion related to surge–sway movement.

Figure 10 investigates the impact of sinusoidal yaw motion with a reduced frequency of 0.6 and an amplitude of 2° on the wake, measured by Fontanella et al. (2025b) at a downstream distance of $3D$, and on the loads of WT2 placed in different positions relative to WT1 (loads were not measured in the 4D configuration).

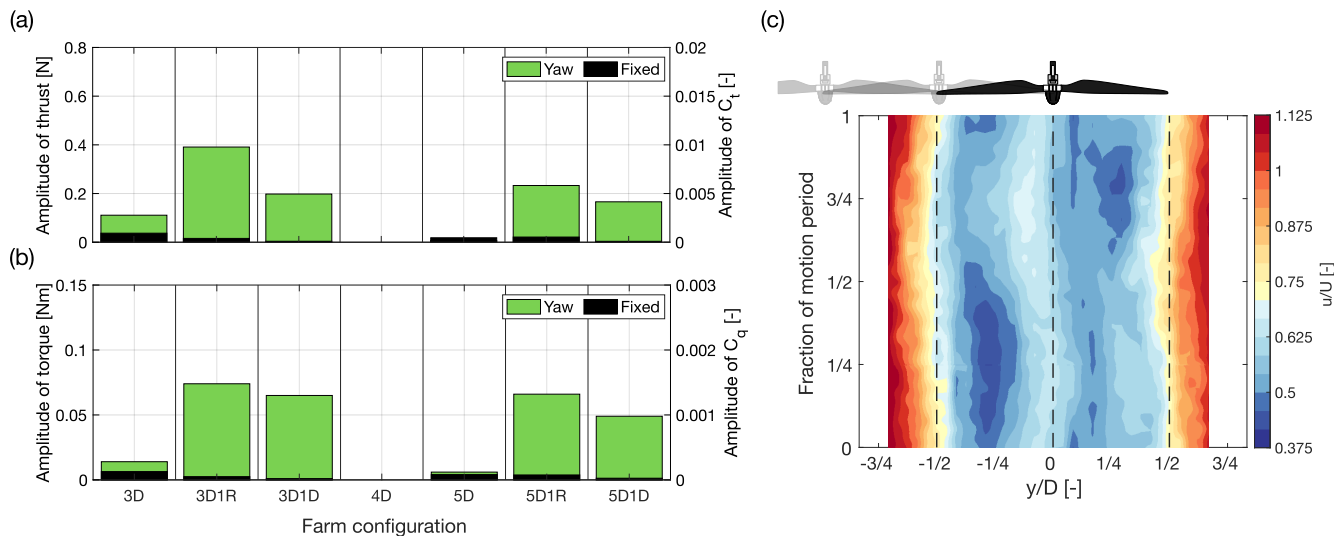


Figure 10. Effect of wake meandering induced by platform yaw motion with 2° amplitude and a reduced frequency 0.6 on the loads of a downstream wind turbine operating in the wake, at varying downstream distances and crosswind positions. (a): amplitude of thrust oscillations on the downstream turbine. (b): amplitude of torque oscillations on the downstream turbine. (c): phase-averaged velocity in the wake of the upstream turbine caused by yaw motion at a downstream distance of 3 rotor diameters.

Phase-averaged velocity time series at hub height show a coherent lateral displacement of the wake. This is particularly
 560 evident at the wake center, which deviates from the rotor axis and returns to it over the course of one motion period. This
 behavior is linked to the periodic change in rotor orientation relative to the wind, which causes the wake to be deflected
 laterally. In addition, the wake exhibits velocity variations that are out of phase on opposite sides. At any given moment, one
 side of the wake shows a velocity minimum while the other side exhibits a maximum. This alternating pattern is strongly
 565 correlated across the wake width and remains synchronized with the platform yaw motion, reflecting the effect of dynamic
 yaw, which creates an apparent wind speed with opposite signs on either side of the rotor.

When WT2 is aligned with WT1 (in the 3D and 5D configurations), opposite sides of its rotor experience velocity fluctuations
 of opposite sign: one side sees a slight increase while the other sees a decrease. These local variations largely cancel in the
 rotor-averaged thrust and torque, so the net oscillations remain small and comparable to those caused by inflow turbulence in
 the fixed-WT1 case. In this configuration, the unsteady wake primarily produces asymmetric loading across the rotor, which
 570 would manifest as side-to-side force and moment fluctuations rather than as significant thrust or torque variations. When WT2
 is laterally offset (by $1R$ or $1D$), this symmetry is broken: part of the rotor is exposed to the unsteady wake while the rest

operates in undisturbed inflow. The lack of cancellation leads to stronger thrust and torque oscillations. In the 1R case, about half of the rotor is immersed in the fluctuating wake, producing substantial unbalanced loads, while in the 1D case only the outer portion is affected, leading to a smaller load response than in the 1R case. In the 3D1R configuration, WT2 experiences zero-to-peak thrust variations of 0.4 N (equivalent to 20.3 kN at full scale) and torque variations of 0.074 Nm (281.2 kNm at full scale). These values are comparable to the load fluctuations observed in the 3D aligned configuration when WT1 undergoes pitch motion with an amplitude of 1.3° and a reduced frequency of 0.6. This indicates that a downstream turbine can experience similar dynamic loading whether it is fully immersed in a pulsating wake induced by pitch motion or partially exposed to a laterally meandering wake caused by yaw motion.

580 3.2.4 Crosswind motion

Figure 11 illustrates the effect of sinusoidal surge–sway motion at various angles γ and with $f_r = 0.6$ on the wake at a downstream distance of $3D$, measured with hot-wire probes as described in Fontanella et al. (2025b), as well as on the aerodynamic loads of WT2 placed at different positions relative to WT1 (loads were not measured for the 4D configuration). When $\gamma = 0^\circ$, the motion corresponds to pure surge, producing velocity oscillations concentrated in the center of the wake. As the motion angle increases, the wake exhibits more pronounced lateral meandering, similar to what is observed in yaw motion. This phenomenon is especially pronounced at $\gamma = 90^\circ$, where the peak in relative velocity at the center of the wake alternates between the two sides of the rotor.

In the farm configuration with aligned turbines at a distance of $3D$, the amplitude of WT2 load oscillations at the platform motion frequency decreases as the motion angle γ increases. This trend reflects a shift from wake pulsation to lateral meandering. As explained in the yaw motion case, meandering-induced velocity fluctuations tend to cancel out across the rotor when the turbines are aligned, reducing dynamic thrust and torque variations. At $5D$ spacing, this behavior is less pronounced: the dynamic loads on WT2 remain nearly constant for motion angles up to 45° but show a noticeable increase at $\gamma = 90^\circ$. This rise in loading is likely due to pure sway motion which induces strong velocity oscillations in the wake that do not fully cancel out across the rotor.

In farm configurations where WT2 is laterally offset, the trend of loads reverses compared to aligned configurations. Here, the amplitude of dynamic loads increases with the motion angle, as only a portion of WT2 rotor is exposed to the periodic lateral wake meandering. As in the yaw motion case, the dynamic loads are higher in the 1R configurations than in the 1D configurations, reflecting the greater extent of rotor-wake interaction. In the 3D1R configuration, when WT1 undergoes motion at a 30° angle to the wind direction, WT2 experiences zero-to-peak thrust variations of 0.37 N (18.7 kN at full scale) and torque variations of 0.064 Nm (243.2 kNm at full scale). These values are similar to load fluctuations seen in the 3D aligned configuration with pitch motion and in the 3D1R configuration with yaw motion.

The load amplitudes during cross-wind motions reach their maximum when WT1 moves orthogonally to the wind direction ($\gamma = 90^\circ$), with thrust variations of 0.61 N (30.9 kN at full scale) and torque variations of 0.109 Nm (418.1 kNm at full scale).

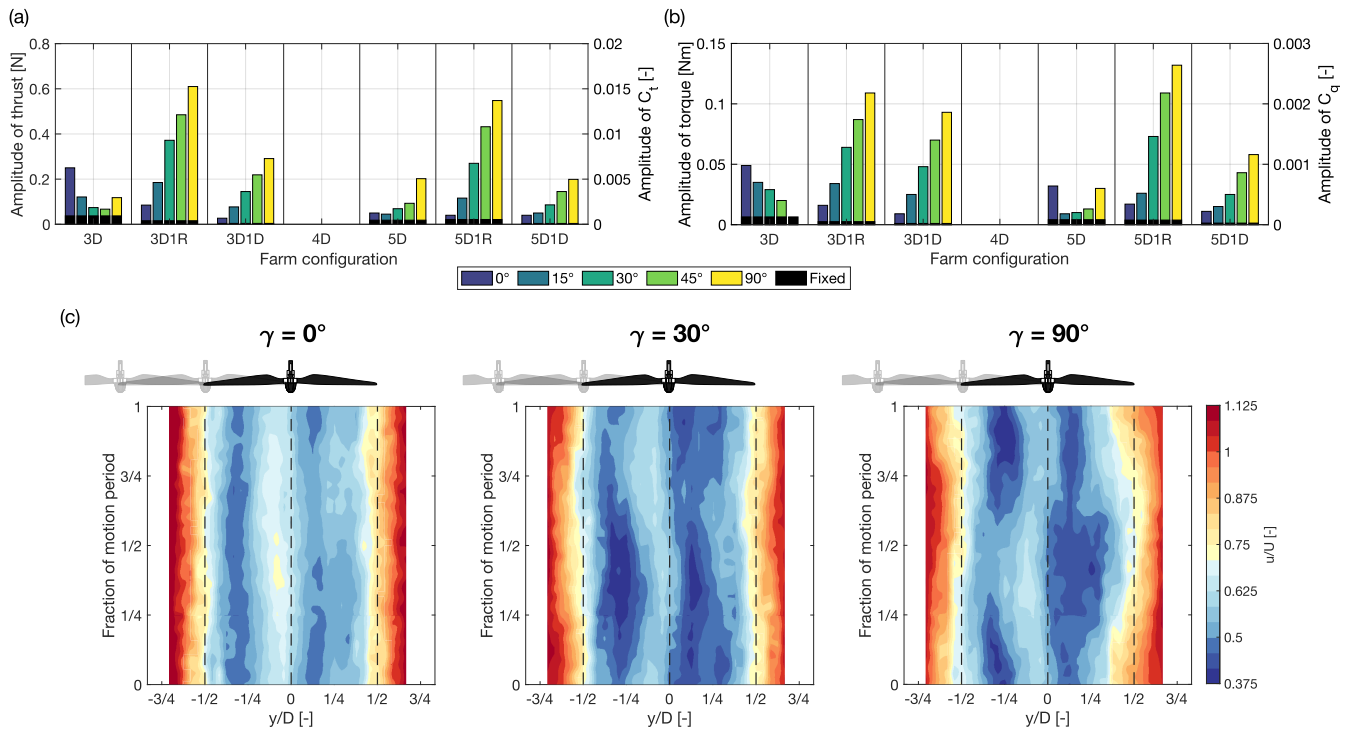


Figure 11. Effect of wake meandering induced by platform translational motion with 0.032 m amplitude (model scale), a reduced frequency 0.6 and various angles relative to the wind direction on the loads of a downstream wind turbine operating in the wake, at different downstream distances and crosswind positions. **(a):** amplitude of thrust oscillations on the downstream turbine. **(b):** amplitude of torque oscillations on the downstream turbine. **(c):** phase-averaged velocity in the wake of the upstream turbine at a downstream distance of 3 rotor diameters for a translational motion at different angles γ relative to the wind direction.

3.2.5 Dynamic loads with irregular waves

605 Sinusoidal motion-platform motions of the upstream wind turbine ~~along individual directions produces~~ produce distinct dynamic loads on a downstream turbine operating in its wake. When WT1 undergoes wave-induced motion, it experiences simultaneous movements in all six degrees of freedom across a broad frequency range. The tests with wave-driven motions aim to assess whether the observations made under sinusoidal motion still hold in these more complex and realistic scenarios.

Figure 12 analyzes the effect of wave-driven motion on the thrust force spectrum of WT2, considering different wind farm 610 configurations and wave headings of 0° and 30° relative to the wind direction.

In the cases with WT1 fixed, the thrust spectrum of WT2 is lowest when it is laterally offset by $1D$ from WT1. The downstream turbine operates mostly outside the wake, experiencing minimal influence from turbulence in the wake of the upstream turbine. In the aligned configuration and with a lateral offset of $1R$, the thrust spectrum is noticeably higher as wake interactions are stronger.

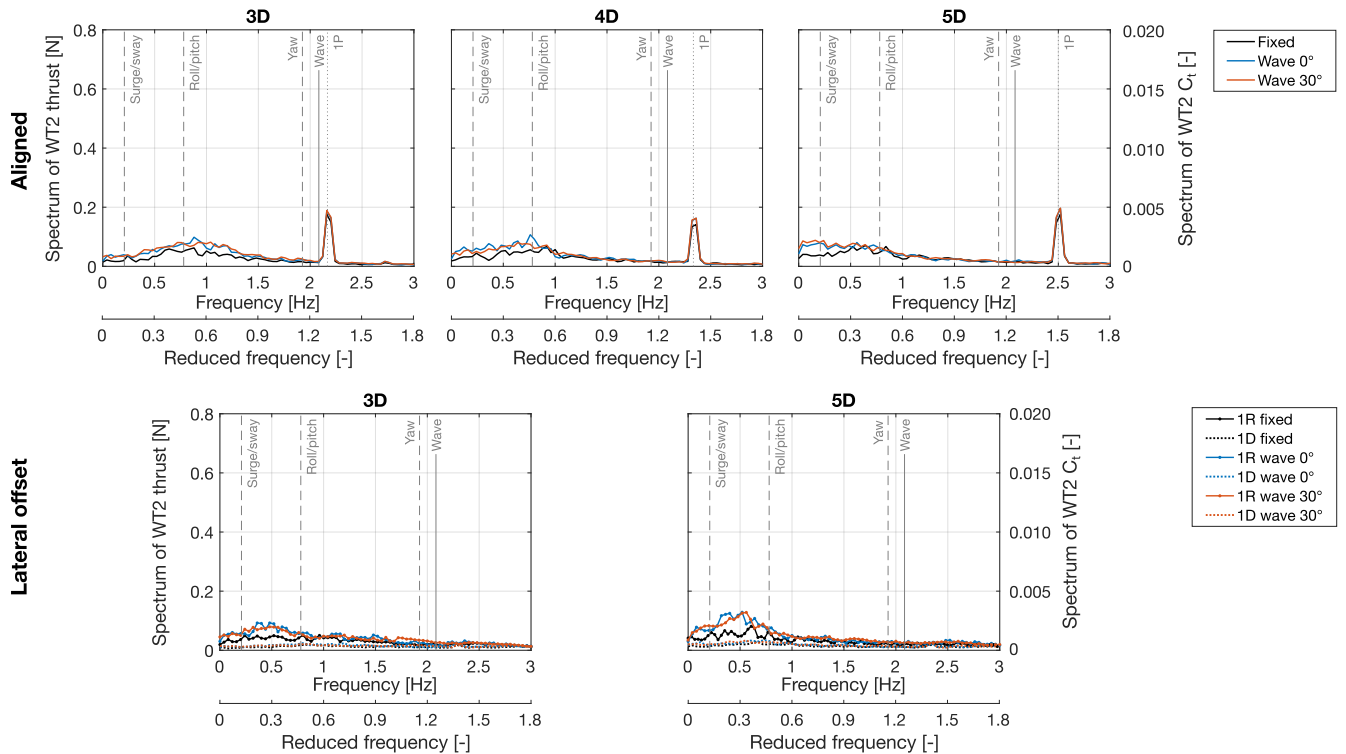


Figure 12. Spectrum of the thrust force on a downstream wind turbine operating at various positions in the wake of an upstream turbine subjected to wave-induced motions. The motions correspond to those of the SOFTWIND 10 MW floating wind turbine under irregular waves with a significant wave height of 5 m and a peak period of 12 s (full scale). The vertical dashed lines mark the natural frequencies of the upstream wind turbine rigid-body modes, the solid vertical line indicates the frequency associated with the peak wave period, and the dotted vertical line corresponds to the rotor rotation frequency of WT2 (1P).

615 When WT1 was subjected to wave-induced motion, the thrust spectrum of WT2 increased at reduced frequencies below 0.6 in both the aligned and 1R configurations. This indicates that upstream platform motions occurring near the surge/sway and roll/pitch natural frequencies contribute to dynamic loading of the downstream turbine in these layouts. The increase was similar for both wave headings (0° and 30°), suggesting limited directional sensitivity under the tested conditions.

620 Across all farm configurations, no increase in load amplitude was observed at frequencies near the spectral peak of the irregular waves (corresponding to a reduced frequency of approximately 1.25), despite the significant amplitude of platform motions occurring at this frequency (see Fig. 3). This result aligns with previous sinusoidal motion tests, which demonstrated that motions at reduced frequencies around 1.2 do not lead to appreciable load oscillations on the downstream turbine.

625 To facilitate comparison with sinusoidal cases, the amplitude of the WT2 thrust spectrum in the irregular wave case was evaluated at a reduced frequency of 0.6 for the 3D configuration. With upstream motion driven by 0° waves, which excite primarily surge and pitch motions, the thrust spectral amplitude increased from 0.05 N (2.5 kN at full scale) in the fixed-WT1

case to 0.08 N (4.1 kN at full scale) under wave-induced motion. However, this remains substantially lower than the dynamic loads induced by prescribed sinusoidal motion: WT2 experienced zero-to-peak thrust fluctuations of 0.25 N (12.7 kN at full scale) with sinusoidal surge at $f_r = 0.6$, and 0.4 N (20.3 kN at full scale) with sinusoidal pitch at the same frequency. These comparisons highlight the more moderate impact of wave-driven motion on the dynamic loading of a downstream turbine
630 compared to idealized, high-amplitude sinusoidal movements.

In cases with a lateral offset of $1R$, the increase in WT2 thrust spectrum relative to the fixed case was more pronounced than in the aligned cases, particularly at reduced frequencies below 0.5. At frequencies above 0.6, the spectrum remained nearly unchanged. In configurations with a $1D$ lateral offset, the influence of wave-induced motion on WT2 thrust oscillations was minimal, confirming that the rotor was largely outside the region affected by the wake.

635 4 Discussion

The analysis of aerodynamic loads from the two wind turbines was carried out from two complementary perspectives: the effect on average performance, particularly the power extracted by the downstream turbine, and the influence on dynamic thrust and torque experienced by the downstream rotor.

In the low-turbulence, short-spacing conditions considered in the experiment (3-to-5 rotor diameters), large, low-frequency
640 motions of the upstream rotor were found to modestly enhance the power extracted by the downstream turbine. These enhancements were particularly pronounced when the upstream turbine underwent sinusoidal motions in yaw or crosswind directions. In ~~one case~~two cases with aligned turbines, WT2 power increased by 26% over the fixed-turbine baseline, ~~though this translated but this corresponded~~ to only a ~~2-2-3.5 W~~ (0.3-0.5 MW at full scale) ~~increase in absolute terms~~absolute gain. Similarly, in partially offset ~~configurations~~layouts, surge-sway motions ~~led to power yielded~~ increases of up to 5.4~~W~~ ~~(equivalent to W~~ (0.82 MW at full scale). These modest absolute gains are explained by the highly persistent wake generated by the low-turbulence inflow and the high thrust of the upstream turbine, which resulted in very low baseline power for WT2 in the fixed case.

However, the power gains observed under idealized sinusoidal motion were only partially reproduced in tests involving realistic wave-driven platform motions of a 10 MW spar floating wind turbine. In particular, wave excitation aligned with the
650 wind direction (0° heading), which excited pitch motion, resulted in downstream power gains similar to those observed under prescribed sinusoidal pitch motion. In contrast, wave excitation at 30° incidence, which introduces combined crosswind and yaw motions, did not consistently lead to power increases in the downstream turbine. This differs from the sinusoidal motion tests, where motions in the yaw and crosswind directions were generally associated with improvements in wake recovery and power output. These results suggest that the irregularity, phase coupling, and lower coherence of real platform responses may
655 limit the effectiveness of wake recovery mechanisms that appear more pronounced under idealized, single-degree-of-freedom sinusoidal motions.

It should be noted that in the wind tunnel the inflow velocity at the turbines is partly influenced by blockage, since the flow is laterally constrained and cannot fully expand around the rotors as it does in the atmosphere. Nevertheless, the relative

differences in WT2 power between fixed and moving WT1 remain directly attributable to the motion-induced wake dynamics, 660 as all configurations were tested under the same wind tunnel conditions. The blockage effect therefore does not affect the comparative conclusions of this study, but it should be considered when extrapolating absolute performance levels to full-scale conditions.

Regarding dynamic loading, sinusoidal motion tests clearly showed that the frequencies of upstream turbine motion were directly reflected in the aerodynamic loads on the downstream rotor, with a well-defined periodic response. The magnitude 665 of these dynamic loads depended on turbine distance, lateral offset, and the type of motion of the upstream wind turbine. For instance, load fluctuations reached up to 12% of the mean torque and 3% of the mean thrust when WT2 operated fully within the wake of WT1, which was undergoing motion aligned with wind (surge or pitch), resulting in wake pulsation. Comparable load amplitudes were also observed when WT2 was only partially immersed in a laterally-meandering wake, generated by crosswind or yaw motions of WT1. Both wake pulsing and meandering can induce substantial cyclic loading; pulsing predominantly in 670 fully aligned turbine configurations, and meandering when there is a lateral offset between the turbines. In real operating conditions, the first scenario is likely to occur when waves are aligned with the wind, exciting surge and pitch motions, and when wind is aligned to wind farm rows placing downwind turbines directly in the full wake of upstream machines. The second scenario may arise under significant wind-wave misalignment and when the wind approaches the wind farm at an angle, resulting in partial wake exposure for downstream turbines and increased wake meandering due to lateral or yaw-induced 675 motion.

Irregular wave-induced motions reproduced these dynamics with broader spectral content and lower amplitude. The key behaviors, such as increased load oscillations for the downstream turbine at low frequencies, persisted although the absolute loading levels were smaller than in sinusoidal tests.

These results suggest a tradeoff: platform motions can promote modest energy gains downstream but also introduce addi- 680 tional cyclic loading. Whether this tradeoff remains in high-turbulence atmospheric conditions or with greater turbine spacing or with dynamic blade pitch and generator torque control remains an open question. In more realistic atmospheric conditions, turbulence is expected to become the dominant driver of wake behavior, including mixing, recovery, and meandering (Wu and Porté-Agel, 2012; Hodgson et al., 2023).

It is also important to note that in this study only the upstream turbine was subjected to motion, while the downstream one 685 remained fixed. In reality, both turbines in a floating array will experience platform motion induced by waves and wind. If the downstream turbine also undergoes motion, its aerodynamic loading will be affected not only by the wake fluctuations generated by the upstream turbine but also by its own platform kinematics. The phasing between the velocity oscillations in the wake and the motion of the downstream rotor may play a critical role: depending on whether the downstream turbine moves in phase or out of phase with the wake fluctuations, the aerodynamic loads can be amplified or mitigated. Moreover, the motions 690 of neighboring turbines are not independent, since wave forcing is spatially correlated as waves propagate across the farm. Such correlated motions could further influence wake–motion interactions. While these coupled effects are beyond the scope of the present work, they highlight the need to account for wave propagation and correlated turbine responses in future studies.

Finally, further research is needed to assess the validity of the conclusions of this work when the downstream turbine is located at larger distances from the upstream one and when static rotor inclination alters the effective swept area or deflects the wake vertically, as these effects were not captured in the present experimental setup.

5 Conclusions

This study investigated, through wind tunnel experiments, how the motion of a floating wind turbine affects the performance and dynamic loading of a downstream turbine operating in its wake. The upstream turbine was subjected to controlled platform motions, both sinusoidal and wave-induced, while the downstream turbine remained fixed and was tested in different relative positions.

In low-turbulence conditions and short ~~spacing~~ turbine spacings (3–5 rotor diameters), large-amplitude, low-frequency motions of the upstream turbine, especially in yaw and crosswind directions, ~~led to~~ produced moderate increases in the power output of the downstream turbine. In the most favorable cases, ~~power increased by the downstream turbine gained~~ up to 26% over the fixed case, although absolute gains remained limited relative to the fixed-turbine baseline, ~~although the corresponding absolute increase remained limited due to the very low baseline power associated with the persistent wake of the upstream turbine.~~ These gains were most evident in sinusoidal tests and ~~only partially reflected in~~ were only partially reproduced under realistic wave-induced motion scenarios.

At the same time, upstream platform motion introduced periodic flow disturbances that propagated downstream and increased dynamic loading on the waked turbine. The magnitude and frequency content of these dynamic loads depended on the type of motion, relative turbine positioning, and turbine-to-turbine distance. Load oscillations reached up to 12% of the mean torque and 3% of the mean thrust in certain farm configurations, with wake pulsing induced by along-wind motions and lateral wake meandering driven by crosswind and yaw motions both contributing similarly to the cyclic loading of the downstream turbine. Key patterns in the aerodynamic loads of the downstream wind turbine identified under sinusoidal motion were also evident in tests involving realistic wave-induced motion. However, the amplitudes of the resulting loads were lower, reflecting the broader frequency content of wave-driven platform response and its interaction with the turbine wake.

Overall, platform-induced wake dynamics can modestly enhance energy capture but also introduce increased cyclic loads. Sinusoidal motion tests are effective for isolating key wake mechanisms, while tests with wave-driven motions provide a more realistic assessment of performance and loading.

Further studies are needed to assess whether the trends observed in this work persist under higher-turbulence inflows and when multiple turbines are in motion. However, the findings of this study clearly underline the importance of considering wake–motion coupling in the design and analysis of future floating wind farms.

Data availability. Measurements of the upstream wind turbine wake under various platform motions are available at <https://doi.org/10.5281/zenodo.13994980>. Load measurements for two wind turbines in various farm setups and motion conditions, including those not covered here, are available at <https://doi.org/10.5281/zenodo.15582187>.

725 **Appendix A: Aerodynamic performance of the model rotor**

The aerodynamic performance of the scale model rotor was evaluated in a steady and uniform wind field with a turbulence intensity of 1.5%, matching the free-stream inflow conditions of the rest of this study. Measurements were performed at a constant blade pitch angle of 0° , while the tip-speed ratio was varied by adjusting the rotor speed at a fixed free-stream wind speed of 4 ms^{-1} .

730 Figure A1 reports the measured thrust coefficient (C_t) and power coefficient (C_p) as functions of tip-speed ratio both with and without blockage correction. The blockage correction was performed using Glauert's wind tunnel interference model presented by Inghels (2013). The correction defines an increment to the free-stream wind speed. The increased wind speed is then used for the computation of the performance coefficients. The wind speed correction depends on the ratio between the rotor-swept area and the wind tunnel cross-section, as well as on the turbine thrust coefficient.

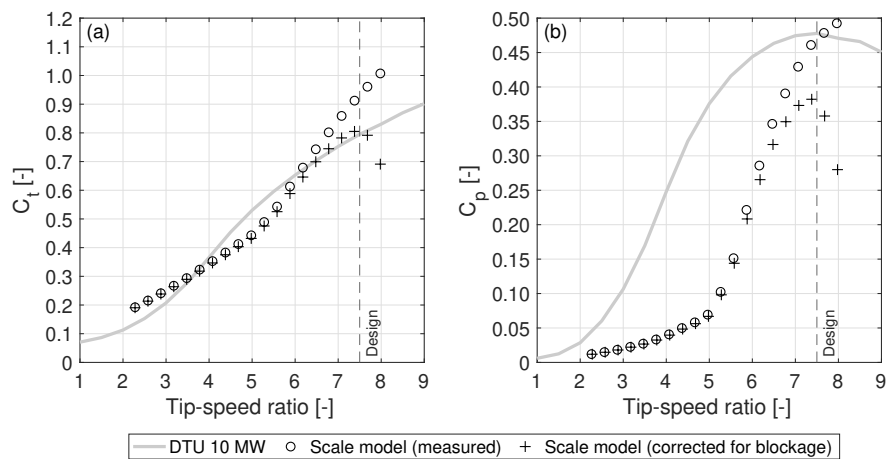


Figure A1. Thrust (C_t) and power (C_p) coefficients of the rotor at different tip-speed ratios. The dashed vertical line indicates the design tip-speed ratio of 7.5.

735 After correction, the model rotor C_t closely matches the DTU 10 MW reference turbine near the design tip-speed ratio of 7.5. The C_p curve has a comparable shape to that of the reference turbine, but its maximum value is lower (0.38 vs. 0.48). This reduction is attributed to the lower efficiency of airfoils at low Reynolds numbers, which is only partially mitigated by the use of a low-Reynolds airfoil in the scale model blades.

In the main body of the paper, performance results are reported without blockage correction, since available correction methods are not applicable to downstream turbines operating in wakes.

740

Appendix B: Rotor effective wind speed estimator

The rotor-effective wind speed (U_{RE}) was estimated from measured thrust using a calibrated thrust–rotor speed–wind speed relation. Thrust was preferred over power as the feedback variable because it is less sensitive to Reynolds number effects at model scale.

745 The estimator relies on a pre-computed thrust map $F_x(\omega, U)$ obtained from a blade-element momentum (BEM) model of the rotor, previously validated against wind-tunnel measurements (Bergua et al., 2023), where it showed excellent agreement with the measured thrust and power characteristics. The model was simulated under steady and uniform inflow for a range of wind speeds U and rotor speeds ω , providing the corresponding steady thrust force F_x .

During the experiments, the rotor speed and thrust signals were averaged over the acquisition window to obtain the mean 750 rotor speed ω_m and mean thrust force $F_{x,m}$. The pair $(\omega_m, F_{x,m})$ was then used to invert the pre-computed thrust map and estimate the corresponding rotor-effective wind speed:

$$U_{RE} = F_x^{-1}(\omega_m(t), F_{x,m}(t)) \quad (B1)$$

where $F_x^{-1}(\cdot)$ denotes the inversion of the thrust map. This process is illustrated in Fig. B1.

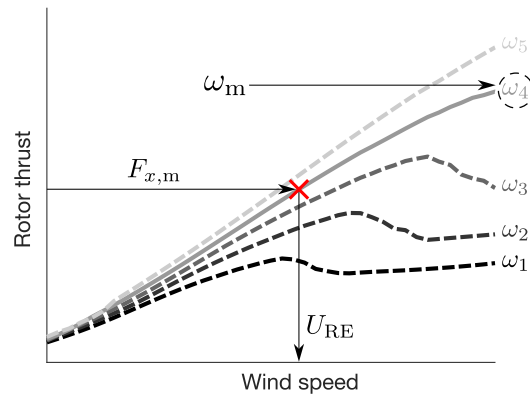


Figure B1. Estimation of rotor-effective wind speed (U_{RE}) by inverting the BEM-based thrust map $F_x(\omega, U)$. The measured mean thrust $F_{x,m}$ and rotor speed ω_m define a unique operating point (red marker) from which U_{RE} is obtained.

Appendix C: Power of the downstream turbine for all motion cases and farm configurations

755 This appendix provides the complete set of time-averaged power measurements for all wind farm configurations and motion scenarios investigated in this study. Because the rotor speed was prescribed and constant in each farm configuration, the aerodynamic power of both turbines was obtained directly from the measured torque and the known rotational speed. In all tests, WT1 operated at a fixed rotor speed of 240 rpm and maintained a time-averaged power output of 72 W (10.93 MW at full scale). The power of WT2 depended on the farm configuration and on its position relative to WT1.

760 Table C1 reports the time-averaged WT2 power for the fixed-tower-base condition across all configurations, together with the fixed rotor speeds at which WT2 was operated. For each configuration, the table also lists the minimum and maximum WT2 power recorded over the repeated tests. The power ratio is defined as the ratio between the WT2 and WT1 power.

Table C1. Time-averaged power output of WT2 for the fixed-tower-base condition across the different farm configurations. WT2 was operated at fixed rotor speeds. Values in brackets indicate the minimum and maximum WT2 power recorded over the tests, along with the corresponding minimum and maximum power ratios when normalized by the average power of WT1.

<u>Configuration</u>	<u>Rotor speed [rpm]</u>	<u>Power [W]</u>	<u>Power ratio [-]</u>
<u>3D</u>	<u>130</u>	<u>7.7 [6.7, 8.2]</u>	<u>0.11 [0.09, 0.12]</u>
<u>3D1R</u>	<u>190</u>	<u>37.1 [35.4, 38.8]</u>	<u>0.52 [0.49, 0.54]</u>
<u>3D1D</u>	<u>220</u>	<u>86.1 [83.6, 88.5]</u>	<u>1.20 [1.16, 1.23]</u>
<u>4D</u>	<u>140</u>	<u>11.1 [9.7, 11.8]</u>	<u>0.15 [0.14, 0.16]</u>
<u>5D</u>	<u>150</u>	<u>13.8 [12.8, 14.6]</u>	<u>0.19 [0.18, 0.20]</u>
<u>5D1R</u>	<u>190</u>	<u>42.6 [41.1, 43.9]</u>	<u>0.59 [0.57, 0.61]</u>
<u>5D1D</u>	<u>190</u>	<u>92.9 [91.0, 93.0]</u>	<u>1.29 [1.26, 1.30]</u>

765 WT1 sinusoidal motions were tested using different combinations of amplitudes and frequencies for each wind farm configuration. Table C2 reports the corresponding time-averaged WT2 power in the case of surge motion, Table C3 for pitch motion, Table C4 for yaw motion, and Table C5 for combined surge–sway motion. In these tables, the power ratios that exceed the maximum ratio observed in the fixed-tower-base case (Table C1) are highlighted.

Table C2. Time-averaged power output of WT2 for the different farm configurations under surge motion of WT1. WT2 was operated at a fixed rotor speed, set according to each farm configuration.

Configuration	Reduced frequency (f_r) [-]	Motion amplitude (a_m) [m]	Rotor speed [rpm]	Power [W]	Power ratio [-]	Variation w.r.t. fixed
3D	0.3	0.064	130	6.7	0.09	-14%
	0.6	0.032	130	6.7	0.09	-14%
	1.2	0.016	130	6.7	0.09	-14%
3D1R	0.3	0.064	190	39.0	0.54	+5%
	0.6	0.032	190	39.0	0.54	+5%
	1.2	0.016	190	38.9	0.54	+5%
3D1D	0.3	0.064	220	83.7	1.16	-3%
	0.6	0.032	220	83.6	1.16	-3%
	1.2	0.016	220	83.5	1.16	-3%
4D	0.3	0.064	140	11.4	0.16	+3%
	0.6	0.032	140	11.3	0.16	+2%
	1.2	0.016	140	11.4	0.16	+3%
5D	0.3	0.064	150	13.3	0.19	-4%
	0.6	0.032	150	12.5	0.17	-10%
	1.2	0.016	150	12.4	0.17	-10%
5D1R	0.3	0.064	190	44.9	0.62	+5%
	0.6	0.032	190	44.7	0.62	+5%
	1.2	0.016	190	44.6	0.62	+5%
5D1D	0.3	0.064	230	92.9	1.29	0%
	0.6	0.032	230	92.6	1.29	0%
	1.2	0.016	230	92.5	1.29	0%

Table C3. Time-averaged power output of WT2 for the different farm configurations under pitch motion of WT1. WT2 was operated at a fixed rotor speed, set according to each farm configuration.

<u>Configuration</u>	<u>Reduced frequency (f_r) [-]</u>	<u>Motion amplitude (a_θ) [°]</u>	<u>Rotor speed [rpm]</u>	<u>Power [W]</u>	<u>Power ratio [-]</u>	<u>Variation w.r.t. fixed</u>
<u>3D</u>	<u>0.3</u>	<u>2.5</u>	<u>130</u>	<u>8.2</u>	<u>0.11</u>	<u>+6%</u>
	<u>0.6</u>	<u>1.3</u>	<u>130</u>	<u>7.3</u>	<u>0.10</u>	<u>-6%</u>
	<u>1.2</u>	<u>0.6</u>	<u>130</u>	<u>9.2</u>	<u>0.13</u>	<u>+19%</u>
<u>3D1R</u>	<u>0.3</u>	<u>2.5</u>	<u>190</u>	<u>39.0</u>	<u>0.54</u>	<u>+5%</u>
	<u>0.6</u>	<u>1.3</u>	<u>190</u>	<u>37.5</u>	<u>0.52</u>	<u>+5%</u>
	<u>1.2</u>	<u>0.6</u>	<u>190</u>	<u>38.8</u>	<u>0.54</u>	<u>+5%</u>
<u>3D1D</u>	<u>0.3</u>	<u>2.5</u>	<u>220</u>	<u>83.5</u>	<u>1.16</u>	<u>-3%</u>
	<u>0.6</u>	<u>1.3</u>	<u>220</u>	<u>85.5</u>	<u>1.19</u>	<u>-1%</u>
	<u>1.2</u>	<u>0.6</u>	<u>220</u>	<u>87.6</u>	<u>1.22</u>	<u>+2%</u>
<u>4D</u>	<u>0.3</u>	<u>2.5</u>	<u>140</u>	<u>11.8</u>	<u>0.16</u>	<u>+6%</u>
	<u>0.6</u>	<u>1.3</u>	<u>140</u>	<u>10.3</u>	<u>0.14</u>	<u>-7%</u>
	<u>1.2</u>	<u>0.6</u>	<u>140</u>	<u>12.1</u>	<u>0.17</u>	<u>+9%</u>
<u>5D</u>	<u>0.3</u>	<u>2.5</u>	<u>150</u>	<u>15.5</u>	<u>0.22</u>	<u>+13%</u>
	<u>0.6</u>	<u>1.3</u>	<u>150</u>	<u>13.6</u>	<u>0.19</u>	<u>-1%</u>
	<u>1.2</u>	<u>0.6</u>	<u>150</u>	<u>13.6</u>	<u>0.19</u>	<u>-2%</u>
<u>5D1R</u>	<u>0.3</u>	<u>2.5</u>	<u>190</u>	<u>44.8</u>	<u>0.62</u>	<u>+5%</u>
	<u>0.6</u>	<u>1.3</u>	<u>190</u>	<u>42.8</u>	<u>0.59</u>	<u>+1%</u>
	<u>1.2</u>	<u>0.6</u>	<u>190</u>	<u>46.2</u>	<u>0.64</u>	<u>+9%</u>
<u>5D1D</u>	<u>0.3</u>	<u>2.5</u>	<u>230</u>	<u>92.2</u>	<u>1.28</u>	<u>-1%</u>
	<u>0.6</u>	<u>1.3</u>	<u>230</u>	<u>89.7</u>	<u>1.25</u>	<u>-4%</u>
	<u>1.2</u>	<u>0.6</u>	<u>230</u>	<u>93.6</u>	<u>1.30</u>	<u>+1%</u>

Table C4. Time-averaged power output of WT2 for the different farm configurations under yaw motion of WT1. WT2 was operated at a fixed rotor speed, set according to each farm configuration.

<u>Configuration</u>	<u>Reduced</u> <u>frequency (f_r) [-]</u>	<u>Motion</u> <u>amplitude (a_θ) [°]</u>	<u>Rotor</u> <u>speed [rpm]</u>	<u>Power</u> <u>[W]</u>	<u>Power ratio</u> <u>[-]</u>	<u>Variation</u> <u>w.r.t. fixed</u>
<u>3D</u>	<u>0.3</u>	<u>2.0</u>	<u>130</u>	<u>9.7</u>	<u>0.13</u>	<u>+26%</u>
	<u>0.6</u>	<u>2.0</u>	<u>130</u>	<u>8.7</u>	<u>0.12</u>	<u>+13%</u>
	<u>1.2</u>	<u>2.0</u>	<u>130</u>	<u>8.4</u>	<u>0.12</u>	<u>+9%</u>
<u>3D1R</u>	<u>0.3</u>	<u>2.0</u>	<u>190</u>	<u>41.2</u>	<u>0.57</u>	<u>+11%</u>
	<u>0.6</u>	<u>2.0</u>	<u>190</u>	<u>39.9</u>	<u>0.55</u>	<u>+8%</u>
	<u>1.2</u>	<u>2.0</u>	<u>190</u>	<u>38.1</u>	<u>0.53</u>	<u>+3%</u>
<u>3D1D</u>	<u>0.3</u>	<u>2.0</u>	<u>220</u>	<u>90.6</u>	<u>1.26</u>	<u>+5%</u>
	<u>0.6</u>	<u>2.0</u>	<u>220</u>	<u>89.5</u>	<u>1.24</u>	<u>+4%</u>
	<u>1.2</u>	<u>2.0</u>	<u>220</u>	<u>88.2</u>	<u>1.22</u>	<u>+2%</u>
<u>5D</u>	<u>0.3</u>	<u>2.0</u>	<u>150</u>	<u>15.6</u>	<u>0.22</u>	<u>+13%</u>
	<u>0.6</u>	<u>2.0</u>	<u>150</u>	<u>13.6</u>	<u>0.19</u>	<u>-2%</u>
	<u>1.2</u>	<u>2.0</u>	<u>150</u>	<u>13.5</u>	<u>0.19</u>	<u>-2%</u>
<u>5D1R</u>	<u>0.3</u>	<u>2.0</u>	<u>190</u>	<u>45.5</u>	<u>0.63</u>	<u>+7%</u>
	<u>0.6</u>	<u>2.0</u>	<u>190</u>	<u>42.8</u>	<u>0.59</u>	<u>0%</u>
	<u>1.2</u>	<u>2.0</u>	<u>190</u>	<u>43.2</u>	<u>0.60</u>	<u>+1%</u>
<u>5D1D</u>	<u>0.3</u>	<u>2.0</u>	<u>230</u>	<u>90.1</u>	<u>1.25</u>	<u>-3%</u>
	<u>0.6</u>	<u>2.0</u>	<u>230</u>	<u>88.6</u>	<u>1.23</u>	<u>-5%</u>
	<u>1.2</u>	<u>2.0</u>	<u>230</u>	<u>89.2</u>	<u>1.24</u>	<u>-4%</u>

Table C5. Time-averaged power output of WT2 for the different farm configurations under surge-sway motion of WT1 (all motions with an amplitude of 0.032 m). WT2 was operated at a fixed rotor speed, set according to each farm configuration.

Configuration	Reduced frequency (f_r) [-]	Motion direction (γ) [°]	Rotor speed [rpm]	Power [W]	Power ratio [-]	Variation w.r.t. fixed
3D	0.6	15	130	8.6	0.12	+11%
	0.6	30	130	8.8	0.12	+14%
	0.6	45	130	9.4	0.13	+22%
	0.6	90	130	8.4	0.12	+8%
3DIR	0.6	15	190	36.9	0.51	-1%
	0.6	30	190	37.3	0.52	0%
	0.6	45	190	42.5	0.59	+15%
	0.6	90	190	40.8	0.57	+10%
3D1D	0.6	15	220	87.3	1.21	+1%
	0.6	30	220	87.2	1.21	+1%
	0.6	45	220	90.0	1.25	+5%
	0.6	90	220	85.9	1.19	0%
5D	0.6	15	150	13.6	0.19	-2%
	0.6	30	150	15.4	0.21	+12%
	0.6	45	150	17.4	0.24	+26%
	0.6	90	150	15.4	0.21	+11%
5DIR	0.6	15	190	44.0	0.61	+3%
	0.6	30	190	44.4	0.62	+4%
	0.6	45	190	47.3	0.66	+11%
	0.6	90	190	45.6	0.63	+7%
5D1D	0.6	15	190	88.4	1.23	-5%
	0.6	30	190	88.1	1.22	-5%
	0.6	45	190	90.7	1.26	-2%
	0.6	90	190	87.5	1.22	-6%

Table C6 reports the time-averaged power of WT2 for the different farm configurations when WT1 was subjected to wave-driven platform motions generated for various wave directions. In these tables, the power ratios that exceed the maximum ratio observed in the fixed-tower-base case (Table C1) are highlighted.

Table C6. Time-averaged power output of WT2 for the different farm configurations under wave-driven motions of WT1 caused by waves from different directions. WT2 was operated at a fixed rotor speed, set according to each farm configuration.

<u>Configuration</u>	<u>Wave direction [°]</u>	<u>Rotor speed [rpm]</u>	<u>Power [W]</u>	<u>Power ratio [-]</u>	<u>Variation w.r.t. fixed</u>
<u>3D</u>	<u>0</u>	<u>130</u>	<u>9.6</u>	<u>0.13</u>	<u>+24%</u>
	<u>30</u>	<u>130</u>	<u>8.9</u>	<u>0.12</u>	<u>+15%</u>
<u>3D1R</u>	<u>0</u>	<u>190</u>	<u>40.4</u>	<u>0.56</u>	<u>+9%</u>
	<u>30</u>	<u>190</u>	<u>38.1</u>	<u>0.53</u>	<u>+3%</u>
<u>3D1D</u>	<u>0</u>	<u>220</u>	<u>86.3</u>	<u>1.20</u>	<u>0%</u>
	<u>30</u>	<u>220</u>	<u>85.5</u>	<u>1.19</u>	<u>-1%</u>
<u>4D</u>	<u>0</u>	<u>140</u>	<u>12.5</u>	<u>0.17</u>	<u>+13%</u>
	<u>30</u>	<u>140</u>	<u>12.2</u>	<u>0.17</u>	<u>+10%</u>
<u>5D</u>	<u>0</u>	<u>150</u>	<u>15.5</u>	<u>0.22</u>	<u>+12%</u>
	<u>30</u>	<u>150</u>	<u>14.1</u>	<u>0.20</u>	<u>+2%</u>
<u>5D1R</u>	<u>0</u>	<u>190</u>	<u>41.5</u>	<u>0.58</u>	<u>-2%</u>
	<u>30</u>	<u>190</u>	<u>43.2</u>	<u>0.60</u>	<u>+2%</u>
<u>5D1D</u>	<u>0</u>	<u>190</u>	<u>88.9</u>	<u>1.24</u>	<u>-4%</u>
	<u>30</u>	<u>190</u>	<u>91.3</u>	<u>1.27</u>	<u>-2%</u>

770 *Data availability.* Measurement data of the wind tunnel experiment are accessible at <https://doi.org/10.5281/zenodo.15582187> (Fontanella et al., 2025a).

Author contributions. All authors prepared and conducted the experiment, and analyzed the measurement data. AF wrote the first draft of the article, while all authors contributed to its review and editing. MB, and AB have procured the funding. MB, SM, and AB have supervised the work.

775 *Competing interests.* At least one of the (co-)authors is a member of the editorial board of Wind Energy Science. The peer-review process was guided by an independent editor, and the authors also have no other competing interests to declare.

Financial support. This research has been funded by the European Union – NextGenerationEU, M4C2 I1.1, Progetto PRIN 2022 “NET-TUNO”, Prot. 2022PFLPHS, CUP D53D23003930006.

References

- 780 Angelou, N., Mann, J., and Dubreuil-Boisclair, C.: Revealing inflow and wake conditions of a 6 MW floating turbine, *Wind Energy Science*, 8, 1511–1531, <https://doi.org/10.5194/wes-8-1511-2023>, 2023.
- Arabgolarcheh, A., Micallef, D., and Benini, E.: The impact of platform motion phase differences on the power and load performance of tandem floating offshore wind turbines, *Energy*, 284, 129 271, <https://doi.org/https://doi.org/10.1016/j.energy.2023.129271>, 2023.
- Arnal, V.: Experimental modelling of a floating wind turbine using a “software-in-the-loop” approach, Theses, École centrale de Nantes, <https://theses.hal.science/tel-03237441>, 2020.
- 785 Bak, C., Zahle, F., Bitsche, R., Kim, T., Yde, A., Henriksen, L. C., Hansen, M. H., Blasques, J. P. A. A., Gaunaa, M., and Natarajan, A.: The DTU 10-MW Reference Wind Turbine, danish Wind Power Research 2013; Conference date: 27-05-2013 Through 28-05-2013, 2013.
- Bayati, I., Belloli, M., Bernini, L., and Zasso, A.: Wind Tunnel Wake Measurements of Floating Offshore Wind Turbines, vol. 137, pp. 214–222, <https://doi.org/10.1016/j.egypro.2017.10.375>, 2017a.
- 790 Bayati, I., Belloli, M., Bernini, L., and Zasso, A.: Aerodynamic design methodology for wind tunnel tests of wind turbine rotors, *Journal of Wind Engineering and Industrial Aerodynamics*, 167, 217 – 227, <https://doi.org/https://doi.org/10.1016/j.jweia.2017.05.004>, 2017b.
- Behrens de Luna, R., Perez-Becker, S., Saverin, J., Marten, D., Papi, F., Ducasse, M.-L., Bonnefoy, F., Bianchini, A., and Paschereit, C.-O.: Quantifying the impact of modeling fidelity on different substructure concepts for floating offshore wind turbines – Part 1: Validation of the hydrodynamic module QBlade-Ocean, *Wind Energy Science*, 9, 623–649, <https://doi.org/10.5194/wes-9-623-2024>, 2024.
- 795 Bergua, R., Robertson, A., Jonkman, J., Branlard, E., Fontanella, A., Belloli, M., Schito, P., Zasso, A., Persico, G., Sanvito, A., Amet, E., Brun, C., Campaña Alonso, G., Martín-San-Román, R., Cai, R., Cai, J., Qian, Q., Maoshi, W., Beardsell, A., Pirrung, G., Ramos-García, N., Shi, W., Fu, J., Corniglioni, R., Lovera, A., Galván, J., Nygaard, T. A., dos Santos, C. R., Gilbert, P., Joulin, P.-A., Blondel, F., Frickel, E., Chen, P., Hu, Z., Boisard, R., Yilmazlar, K., Croce, A., Harnois, V., Zhang, L., Li, Y., Aristondo, A., Mendikoa Alonso, I., Mancini, S., Boorsma, K., Savenije, F., Marten, D., Soto-Valle, R., Schulz, C. W., Netzband, S., Bianchini, A., Papi, F., Cioni, S., Trubat, P., Alarcon,
- 800 D., Molins, C., Cormier, M., Brüker, K., Lutz, T., Xiao, Q., Deng, Z., Haudin, F., and Goveas, A.: OC6 project Phase III: validation of the aerodynamic loading on a wind turbine rotor undergoing large motion caused by a floating support structure, *Wind Energy Science*, 8, 465–485, <https://doi.org/10.5194/wes-8-465-2023>, 2023.
- Bossuyt, J., Ferčák, O., Sadek, Z., Meneveau, C., Gayme, D. F., and Cal, R. B.: Floating wind farm experiments through scaling for wake characterization, power extraction, and turbine dynamics, *Phys. Rev. Fluids*, 8, 120 501, <https://doi.org/10.1103/PhysRevFluids.8.120501>,
- 805 2023.
- Carmo, L., Jonkman, J., and Thedin, R.: Investigating the interactions between wakes and floating wind turbines using FAST.Farm, *Wind Energy Science*, 9, 1827–1847, <https://doi.org/10.5194/wes-9-1827-2024>, 2024.
- Chitteth Ramachandran, R., Desmond, C., Judge, F., Serraris, J.-J., and Murphy, J.: Floating wind turbines: marine operations challenges and opportunities, *Wind Energy Science*, 7, 903–924, <https://doi.org/10.5194/wes-7-903-2022>, 2022.
- 810 Firpo, A., Sanvito, A. G., Persico, G., Dossena, V., Schito, P., and Zasso, A.: Multi-fidelity actuator-line modelling of FOWT wakes, *Journal of Physics: Conference Series*, 2767, 052 050, <https://doi.org/10.1088/1742-6596/2767/5/052050>, 2024.
- Fontanella, A., Bayati, I., Mikkelsen, R., Belloli, M., and Zasso, A.: UNAFLOW: a holistic wind tunnel experiment about the aerodynamic response of floating wind turbines under imposed surge motion, *Wind Energy Science*, 6, 1169–1190, <https://doi.org/10.5194/wes-6-1169-2021>, 2021.

- 815 Fontanella, A., Facchinetti, A., Di Carlo, S., and Belloli, M.: Wind tunnel investigation of the aerodynamic response of two 15 MW floating wind turbines, *Wind Energy Science*, 7, 1711–1729, <https://doi.org/10.5194/wes-7-1711-2022>, 2022a.
- Fontanella, A., Zasso, A., and Belloli, M.: Wind tunnel investigation of the wake-flow response for a floating turbine subjected to surge motion, *Journal of Physics: Conference Series*, 2265, 042 023, <https://doi.org/10.1088/1742-6596/2265/4/042023>, 2022b.
- Fontanella, A., Cioni, S., Papi, F., Muggiasca, S., Bianchini, A., and Belloli, M.: NETTUNO Experiment 2 – Ef-
820 fects of floating wind turbine motion on a downstream turbine performance and loads, <https://www.nettuno-project.it>, <https://doi.org/https://doi.org/10.5281/zenodo.15582187>, accessed: 05/06/2025, 2025a.
- Fontanella, A., Fusetti, A., Cioni, S., Papi, F., Muggiasca, S., Persico, G., Dossena, V., Bianchini, A., and Belloli, M.: Wake development in floating wind turbines: new insights and an open dataset from wind tunnel experiments, *Wind Energy Science*, 10, 1369–1387, <https://doi.org/10.5194/wes-10-1369-2025>, <https://wes.copernicus.org/articles/10/1369/2025/>, 2025b.
- 825 Gaertner, E., Rinker, J., Sethuraman, L., Zahle, F., Anderson, B., Barter, G., Abbas, N., Meng, F., Bortolotti, P., Skrzypinski, W., Scott, G., Feil, R., Bredmose, H., Dykes, K., Sheilds, M., Allen, C., and Viselli, A.: Definition of the IEA 15-Megawatt Offshore Reference Wind Turbine, Tech. rep., International Energy Agency, <https://www.nrel.gov/docs/fy20osti/75698.pdf>, 2020.
- Hodgson, E. L., Madsen, M. H. A., and Andersen, S. J.: Effects of turbulent inflow time scales on wind turbine wake behavior and recovery, *Physics of Fluids*, 35, 095 125, <https://doi.org/10.1063/5.0162311>, 2023.
- 830 Inghels, P.: Wind-tunnel blockage corrections for wind-turbine measurements, Tech. rep., Royal Institute of Technology KTH Mechanics, <https://urn.kb.se/resolve?urn=urn:nbn:se:kth:diva-138602>, 2013.
- Jonkman, B., Mudafort, R. M., Platt, A., Branlard, E., Sprague, M., Jonkman, J., Ross, H., Hall, M., Vijayakumar, G., Buhl, M., Bortolotti, P., Ananthan, S., Schmidt, M., Rood, J., Damiani, R., Mendoza, N., Shaler, K., Housner, S., Bendl, K., Carmo, L., Quon, E., Phillips, M. R., Kusuno, N., and Salcedo, A. G.: OpenFAST/openfast: v3.4.1, <https://doi.org/10.5281/zenodo.7632926>, <https://doi.org/10.5281/zenodo.7632926>, 2023.
- 835 Jonkman, J., Butterfield, S., Musial, W., and Scott, G.: Definition of a 5-MW Reference Wind Turbine for Offshore System Development, Tech. rep., National Renewable Energy Laboratory (NREL), Golden, CO., <https://doi.org/10.2172/947422>, <https://www.osti.gov/biblio/947422>, 2009.
- Li, Y., Yu, W., and Sarlak, H.: Wake interaction of dual surging FOWT rotors in tandem, *Renewable Energy*, 239, 122 062, <https://doi.org/https://doi.org/10.1016/j.renene.2024.122062>, 2025.
- 840 Messmer, T., Hölling, M., and Peinke, J.: Enhanced recovery caused by nonlinear dynamics in the wake of a floating offshore wind turbine, *Journal of Fluid Mechanics*, 984, A66, <https://doi.org/10.1017/jfm.2024.175>, 2024a.
- Messmer, T., Peinke, J., and Hölling, M.: Wind tunnel investigation on the recovery and dynamics of the wake of a floating offshore wind turbine subjected to low inflow turbulence, *Journal of Physics: Conference Series*, 2767, 092 083, <https://doi.org/10.1088/1742-6596/2767/9/092083>, 2024b.
- 845 Messmer, T., Peinke, J., Croce, A., and Hölling, M.: The role of motion-excited coherent structures in improved wake recovery of a floating wind turbine, *Journal of Fluid Mechanics*, 1018, A23, <https://doi.org/10.1017/jfm.2025.10509>, 2025.
- Meyers, J., Bottasso, C., Dykes, K., Fleming, P., Gebraad, P., Giebel, G., Göçmen, T., and van Wingerden, J.-W.: Wind farm flow control: prospects and challenges, *Wind Energy Science*, 7, 2271–2306, <https://doi.org/10.5194/wes-7-2271-2022>, 2022.
- 850 Micallef, D. and Rezaeiha, A.: Floating offshore wind turbine aerodynamics: Trends and future challenges, *Renewable and Sustainable Energy Reviews*, 152, 111 696, <https://doi.org/https://doi.org/10.1016/j.rser.2021.111696>, 2021.

- Pagamonci, L., Papi, F., Cojocaru, G., Belloli, M., and Bianchini, A.: How does turbulence affect wake development in floating wind turbines? A critical assessment, *Wind Energy Science Discussions*, 2025, 1–36, <https://doi.org/10.5194/wes-2024-169>, 2025.
- 855 Papi, F., Troise, G., Behrens de Luna, R., Saverin, J., Perez-Becker, S., Marten, D., Ducasse, M.-L., and Bianchini, A.: Quantifying the impact of modeling fidelity on different substructure concepts – Part 2: Code-to-code comparison in realistic environmental conditions, *Wind Energy Science*, 9, 981–1004, <https://doi.org/10.5194/wes-9-981-2024>, 2024.
- Ramos-García, N., González Horcas, S., Pegalajar-Jurado, A., Kontos, S., and Bredmose, H.: Investigation of the floating IEA wind 15-MW RWT using vortex methods Part II: Wake impact on downstream turbines under turbulent inflow, *Wind Energy*, 25, 1434–1463, <https://doi.org/https://doi.org/10.1002/we.2738>, 2022.
- 860 Schulz, C. W., Netzband, S., Özinan, U., Cheng, P. W., and Abdel-Maksoud, M.: Wind turbine rotors in surge motion: new insights into unsteady aerodynamics of floating offshore wind turbines (FOWTs) from experiments and simulations, *Wind Energy Science*, 9, 665–695, <https://doi.org/10.5194/wes-9-665-2024>, 2024.
- Schulz, C. W., Begua, R., Branlard, E., Netzband, S., Jonkman, J., and Roberston, A.: Unsteady Aerodynamics of Large-Scale Floating Offshore Wind Turbines in Surge Motion, Available at SSRN, <https://doi.org/10.2139/ssrn.5375682>, 2025.
- 865 Shen, W. Z. and Mikkelsen, R. F.: Study on wind turbine arrangement for offshore wind farms, in: ICOWEOE-2011, vol. Paper 05, international Conference on Offshore Wind Energy and Ocean Energy, ICOWEOE ; Conference date: 31-10-2011 Through 02-11-2011, 2011.
- Stevens, R. J. A. M., Hobbs, B. F., Ramos, A., and Meneveau, C.: Combining economic and fluid dynamic models to determine the optimal spacing in very large wind farms, *Wind Energy*, 20, 465–477, <https://doi.org/https://doi.org/10.1002/we.2016>, 2017.
- 870 Van Der Hoek, D., Ferreira, C. S., and Van Wingerden, J.-W.: Experimental comparison of induction control methods for wind farm power maximization on a scaled two-turbine setup, *Journal of Physics: Conference Series*, 2767, 092064, <https://doi.org/10.1088/1742-6596/2767/9/092064>, <https://dx.doi.org/10.1088/1742-6596/2767/9/092064>, 2024.
- Van Der Hoek, D., Den Abbeele, B. V., Ferreira, C. S., and van Wingerden, J.-W.: Maximizing wind farm power output with the helix approach: Experimental validation and wake analysis using tomographic particle image velocimetry, *Wind Energy*, 27, 463–482, <https://doi.org/https://doi.org/10.1002/we.2896>, 2024.
- 875 Wu, Y.-T. and Porté-Agel, F.: Atmospheric Turbulence Effects on Wind-Turbine Wakes: An LES Study, *Energies*, 5, 5340–5362, <https://doi.org/10.3390/en5125340>, 2012.